



AMERICAN METEOROLOGICAL SOCIETY

Monthly Weather Review

EARLY ONLINE RELEASE

This is a preliminary PDF of the author-produced manuscript that has been peer-reviewed and accepted for publication. Since it is being posted so soon after acceptance, it has not yet been copyedited, formatted, or processed by AMS Publications. This preliminary version of the manuscript may be downloaded, distributed, and cited, but please be aware that there will be visual differences and possibly some content differences between this version and the final published version.

The DOI for this manuscript is doi: [10.1175/MWR-D-12-00294.1](https://doi.org/10.1175/MWR-D-12-00294.1)

The final published version of this manuscript will replace the preliminary version at the above DOI once it is available.

If you would like to cite this EOR in a separate work, please use the following full citation:

Newman, A., and R. Johnson, 2013: Dynamics of a Simulated North American Monsoon Gulf Surge Event. *Mon. Wea. Rev.* doi:10.1175/MWR-D-12-00294.1, in press.



2

4

6

8

Dynamics of a Simulated North American Monsoon Gulf Surge Event

10

Andrew J. Newman*

Department of Atmospheric Science, Colorado State University, Fort Collins Colorado

12

[†]Current affiliation: National Center for Atmospheric Research, * Boulder Colorado

14

and

16

18

Richard H. Johnson

Department of Atmospheric Science, Colorado State University, Fort Collins Colorado

20

22

24

26

6 March 2013

28

30

32

*The National Center for Atmospheric Research is sponsored by the National Science Foundation

34

36

38

*Corresponding author address: Andrew Newman, National Center For Atmospheric Research, Boulder, CO 80307. E-mail: anewman@ucar.edu

40

ABSTRACT

42

44

Gulf surges are transient disturbances that propagate along the Gulf of California (GoC) from south to north, transporting cool moist air toward the deserts of northwest Mexico and the southwest United States during the North American monsoon. They have been shown to modulate precipitation and have been linked to severe weather and flooding in northern Mexico and the southwest United States. The general features and progression of surge events are well documented but their detailed dynamical evolution is still unclear. In this study, a convection-permitting simulation is performed over the core monsoon region for the 12-14 July 2004 gulf surge event and the dynamics of the simulated surge are examined.

46

48

50

52

Initially, convection associated with the tropical easterly wave precursor to tropical cyclone Blas creates a disturbance in the southern GoC on early 12 July. This disturbance is a precursor to the gulf surge on 13 July and is a *Kelvin shock* (internal bore under the influence of rotation) that dissipates in the central GoC. The surge initiates from inflow from the mouth of the GoC along with convective outflow impinging on the southern GoC. Continued convective outflow along the GoC generates multiple gravity currents and internal bores while intensifying the simulated surge as it propagates up the GoC. As the core of the surge reaches the northern GoC, a Kelvin shock is again the best dynamical fit to the phenomenon. Substantial low-level cooling and moistening are associated with the modeled surge along the northern GoC as is observed.

54

56

58

60

62

64

66 **1. Introduction**

68 Gulf surge events, or surge events for short, are critical transient events in the North
American monsoon (NAM) because they have been tied to moisture flux and precipitation
anomalies during the NAM (Anderson et al. 2000a; Berbery 2001; Douglas and Leal 2003;
70 Gochis et al. 2004; Higgins et al. 2004) and severe weather outbreaks in Arizona (Maddox et al.
1995). Most of the large-scale features associated with the initiation of a surge event were first
72 identified over 35 years ago and have come to a consensus in the literature. Hales (1972) and
Brenner (1974) first introduced the concept of a “surge” of cool moist air providing moisture to
74 the monsoon region from the tropical east Pacific channeled through the Gulf of California
(GoC). Hales (1972) describes several surge events and typical characteristics associated with
76 them. It was also noted that surges are generally associated with some type of cloudy
disturbance south of the GoC as shown satellite imagery (Hales 1972). Brenner (1974)
78 highlights one surge case and notes that easterly waves, tropical cyclones or some other agent
could initiate a surge event. Figure 1 gives a general overview of the NAM region with some
80 relevant features of the surge event examined herein.

More recently, modeling and statistical studies have been performed to determine the
82 causes and evolution characteristics of surge events (Stensrud et al. 1997; Fuller and Stensrud
2000; Anderson et al. 2000b; Higgins and Shi 2005; Adams and Stensrud 2007). Fuller and
84 Stensrud (2000) show that tropical easterly waves (TEWs) are precursors to many surges while
Higgins and Shi (2005) show that tropical cyclones (TCs) moving near the mouth of the GoC
86 lead to a higher occurrence of strong surges. The Madden-Julian Oscillation may even modulate
surge events through its modulation on Eastern Pacific tropical cyclone genesis (Maloney and
88 Hartmann 2000). Bordoni and Stevens (2006) use principal component analysis to show that a

gulf surge mode is the leading EOF in the region during the NAM season and that it relates
90 strongly to TEW passage. The modeling studies of Stensrud et al. (1997) and Adams and
Stensrud (2007) again show that TEWs are associated with surge events in some manner.

92 However, there are a few important aspects of surge events that are still unresolved. The
largest unknown pertains to the dynamics of surge events and their evolution. Since the events
94 occur in a data-sparse region, it has been difficult to unravel what type of phenomena a surge
event is and whether it evolves from one type of system to another (i.e., gravity current to
96 solitary wave) during its lifecycle. Zehnder (2004) examines a detailed list of possible
dynamical mechanisms for surge events, but does not come to a definitive conclusion. Rogers
98 and Johnson (2007), hereafter RJ2007, look at one strong surge event from an observational
standpoint and conclude that an internal bore is the most likely suspect for the initial surge event.
100 Mejia et al. (2010) examine the same surge using aircraft data but cannot reach a definitive
conclusion regarding the surge dynamics. Overall, it is generally thought that gulf surges are
102 likely some type of coastally trapped disturbance (Zehnder 2004; RJ2007), but the specific
dynamical definition of surge events remains unclear.

104 To attempt to more definitively answer what a surge event is and how it evolves
dynamically, a model simulation of a surge event that occurred during the North American
106 Monsoon Experiment (NAME) (Higgins et al. 2006) is examined. This simulation is compared
in detail to NAME observations in Newman and Johnson (2012, hereafter NJ2012) and shows
108 the ability to reproduce observed features of the surge event in a very reasonable manner. The
dynamics of the simulated surge will be discussed to provide a clearer picture of the surge from
110 initiation through its arrival in the Sonoran Desert. A brief description of the model
configuration is followed by an assessment of the dynamics of the simulated surge and finally, a

112 summary discussion.

114 **2. Model configuration**

The Weather Research and Forecasting (WRF) model, Advanced Research WRF (ARW) dynamical core, version 3.2.1 was used in this study (Bruyere et al. 2010). One high-resolution domain (Fig. 2) was used with a domain size of 2000×2320 km and a horizontal grid spacing of 4-km (501×581 points) and 55 vertical levels between the surface and 100 hPa. The vertical grid is stretched such that it has seven levels in the lowest 1 km to a constant Δz of ~340 m in the upper troposphere. This horizontal resolution allows explicit simulation of convective systems, not necessarily convective elements, thus it can be considered convection-permitting (Bryan and Morrison 2012) and no convective parameterization is used. In all simulations the Rapid Radiative Transfer Model longwave, Dudhia shortwave, Thompson et al. (2008) microphysics (with bug fixes to graupel calculations), Noah land surface model, and Quasi-Normal Scale Elimination (QNSE) surface and boundary layer schemes are used (Sukoriansky et al. 2006). The North American Regional Reanalysis (NARR) (Mesinger et al. 2006) was used for initial and boundary conditions and the simulation was initialized at 1200 UTC 11 July and integrated until 0000 UTC 14 July. All analysis begins at 0600 UTC 12 July giving 18 hours of spin-up time for WRF to generate the appropriate higher resolution circulations and precipitation features. See NJ2012 for further discussion of the model configuration.

132 **3. Dynamical Mechanisms**

In an attempt to answer the unresolved question of the dynamical mechanism of the gulf surge, possible theoretical phenomena are compared to the simulated surge feature. Coastally trapped disturbances (CTDs) are disturbances that propagate along topographic barriers that are

136 parallel to the coastline (Durrán 2000). They are characterized by being rotationally trapped
against the topography by Coriolis effects and their amplitude decays away from the coastline
138 (Skamarock 1999; Durrán 2000). The wave amplitude also decays in the vertical as the CTD is
vertically trapped with the trapping mechanism discussed shortly. Many past studies have
140 examined CTDs over various regions of the world and have characterized CTDs as some type of
laterally trapped linear Kelvin wave (with the topography on the right in the Northern
142 Hemisphere), a Kelvin wave modified by a topographically trapped Rossby wave, a Kelvin wave
that has non-linearly steepened into a shock front on the leading edge, or a rotating gravity
144 current (Gill 1977; Dorman 1985; Holland and Leslie 1986; Dorman 1987; Mass and Albright
1987; Reason and Styen 1992; Rogerson and Samelson 1995; Skamarock 1999; Ralph et al.
146 2000; Durrán 2000; Zehnder 2004; RJ2007). It is also possible the surge is an internal bore or
gravity current that is propagating up the GoC with no rotational impacts and therefore not
148 coastally trapped. Thus, there are many plausible dynamical mechanisms of which the following
will be examined herein: gravity currents with/without rotation, internal bores, internal bores
150 with rotation (or Kelvin shocks), topographically trapped Rossby waves, or some type of
coastally trapped Kelvin wave (Gill 1982; Reason and Steyn 1992; Federov and Melville 1996;
152 Skamarock et al. 1999; Helfrich et al. 1999; Durrán 2000; Ralph et al. 2000; Zehnder 2004).

Before delving into the dynamics of the gulf surge event, some background discussion on
154 Kelvin wave and Kelvin shock type CTDs is necessary. In the vertical, a Kelvin wave type CTD
was assumed to be trapped by a strong marine layer inversion present above the boundary layer
156 which allows for use of the shallow water model to explain the dynamics of the CTD (Gill 1977;
Dorman 1985; Holland and Leslie 1986; Reason and Styen 1992; Durrán 2000). However,
158 Durrán (2000) showed that the vertical trapping mechanism of Kelvin wave type CTDs is

actually that the CTDs are sub-inertial and that the terrain is of finite height. A sub-inertial wave
160 is merely a wave with an angular frequency less than Coriolis (Durrán 2000). For a Kelvin wave
to be trapped by the marine layer inversion, the CTD wavelength would need to be typically less
162 than ~5 km (Durrán 2000). Durrán (2000) goes on to term these Kelvin waves as “step-trapped
Kelvin waves” and shows that they are dispersive with phase speed depending on wavelength
164 and also the barrier height and atmospheric stratification. The shallow-water system predicts
non-dispersive Kelvin waves, trapped by the marine layer inversion suggesting that it may not be
166 a good proxy for Kelvin wave type CTDs (Durrán 2000). Therefore, discussion in this study will
focus mainly on step-trapped Kelvin waves when examining the Kelvin wave gulf surge
168 dynamical mechanism.

The term Kelvin shock is introduced by Helfrich et al. (1999) who study non-linear fluid
170 intrusions via a dam break in a rotating channel with a non-zero downstream depth. Kelvin
shocks are essentially internal bores modified by rotation. They are characterized by having the
172 maximum amplitude at the coast, limited offshore distance, across-coast velocities and
propagation speeds very similar to non-rotating internal bores. The shock front can also lag
174 behind the leading edge at the coast depending on channel width and downstream fluid depth
(Helfrich et al. 1999). These Kelvin shocks also transport fluid downstream, an important
176 consideration for gulf surge events (Zehnder 2004). Finally, Kelvin shocks and Kelvin wave
type CTDs will have isentropes that intersect the topography, an important distinction between
178 them and topographically trapped Rossby waves (Zehnder 2004).

Two features, a precursor wave on 12 July 2004 and the initial surge impulse on 13 July
180 are examined in the context of the above dynamical mechanisms. The simulated precursor wave
is generated from a convective cluster related to the precursor tropical wave to tropical storm

182 Blas near the mouth of the GoC just before 10 UTC 12 July. This wave then propagates up the
GoC through ~20-22 UTC washing out between Los Mochis and Bahia Kino (NJ2012). Figure 3
184 gives approximate leading edge locations for the precursor wave at various times on 12 July.
The simulated gulf surge forms early on 13 July and then propagates up the GoC, reaching the
186 northern GoC coastline after 12 UTC (Fig. 3) (NJ2012). The evolution of the surge is complex
and will be discussed in more detail in later sections.

188

a. Precursor Wave

190 1) INITIATION PHASE

The observed and simulated precursor wave on 12 July are thoroughly described in Mejia
192 et al. (2010) and NJ2012. Relevant to this work, the simulated wave originates from a
convectively generated gravity current interacting with the mean stratification over the southern
194 GoC (Fig. 4) (NJ2012). This precursor wave is noted as “structure 2” (S2) while “Structure 1”
(S1) is defined as the convectively generated gravity current in Mejia et al. (2010) and herein.
196 This generation mechanism immediately rules out topographically trapped Rossby waves.
Topographically trapped Rossby waves are larger scale features (~1500 km wavelength)
198 generated by extended periods of downslope, offshore flow interacting with the ambient
atmospheric stratification (Skamarock et al. 1999). In this case the gravity current interacts with
200 the mean stratification over a period of only several hours over the GoC, thus void of an
extended downsloping event. Furthermore, the wavelength of S2 is approximately ~700 km¹,

¹ Estimated from an approximate 6 hour passage time at Los Mochis and an 16 m s⁻¹ phase speed resulting in a half wavelength of ~350 km (following Durran 2000).

202 much less than that of the topographically trapped Rossby waves generated in Skamarock et al.
(1999) or simulated by Zehnder (2004).

204 2) MATURE PHASE

S2 propagates along the GoC and moves ahead of S1 as S1 dissipates (Fig. 4, bottom).
206 The modeled average total system speed from 1200-2000 UTC 12 July is $17.7 \pm 1.8 \text{ m s}^{-1}$. A
mass weighted vertical average of the flow in the region just ahead of S2 is $1.6 \pm 0.5 \text{ m s}^{-1}$ in the
208 direction of propagation of S2 resulting in a modeled intrinsic phase speed of $16.1 \pm 1.9 \text{ m s}^{-1}$.
As S2 passes (starting at 1530 UTC) Los Mochis mean sea level pressure (MSLP) rises in phase
210 with wind speed while the 2 m temperature also increases slightly (not shown). Above the
surface, a shift to southerly or southeasterly winds (and thus moisture flux) and cooling is present
212 behind the leading edge of S2 (Fig. 4, top). The top of S2 roughly aligns with the height of the
SMO, the maximum wind magnitudes are at the coast and the flow is nearly parallel with the
214 coast, but cross-coast flow (toward the SMO) is present throughout the passage of S2 (Fig. 5).
Finally, there is no clear mixed layer capped with an inversion in the lowest 200 hPa, rather the
216 atmosphere is continuously stratified with a Brunt–Väisälä frequency of $\sim 0.015 \text{ s}^{-1}$.

From these characteristics, S2 is clearly not a gravity current with or without rotation.
218 The question then is, what is this phenomenon? Is it a coastally trapped Kelvin wave that can be
described by the shallow-water system (Reason and Styen 1992), a step-trapped Kelvin wave
220 (Durrán 2000), an internal bore (e.g., Klemp et al. 1997), a Kelvin shock (Helfrich et al. 1999),
or some combination of these mechanisms? S2 propagates ahead of S1, with little surface
222 cooling evident in Figs. 4 & 5 or at Los Mochis (LM). Also, using Fig. 4 the estimated
maximum phase speed of S1 is $\sim 12.5 \text{ m s}^{-1}$ ($g' \approx 0.13$, $h \approx 600 \text{ m}$, where $g' = g(\Delta\theta/\theta_o)$)
224 (Benjamin 1968), thus S2 is not a continuation of or tied to S1. In regards to coastally trapped

Kelvin waves, the estimated wavelength of 700 km along with the absence of a clear mixed layer
226 inversion, suggests the classical shallow-water description of Kelvin waves will not adequately
describe the characteristics of S2 as this wave will not be trapped by an inversion layer (Durran
228 2000). Even with the presence of a large boundary layer inversion, the wavelength of S2 along
with the mean Brunt–Väisälä frequency of 0.015 s^{-1} means the inversion will be unable to
230 vertically trap S2 (Durran 2000). Using a representative height of $\sim 1500 \text{ m}$ for the SMO along
the southern and central GoC, a phase speed of $\sim 8.5 \text{ m s}^{-1}$ for a linear step-trapped Kelvin wave
232 could be expected (Durran 2000), around half of the model estimated phase speed. Also, there is
across-coast flow present in S2 (Fig. 5) below the top of the SMO, which is excluded from
234 analysis of linear step-trapped Kelvin waves (Durran 2000). Also note that the wavelength of S2
results in an angular frequency of $\omega_{s2} \approx 1.4 \times 10^{-4} \text{ s}^{-1}$, larger than f at 30° N ($7.3 \times 10^{-5} \text{ s}^{-1}$). Thus it
236 is unlikely that S2 is a step-trapped Kelvin wave.

Internal bores without rotation or Kelvin shocks are the other possible dynamical
238 mechanisms for S2. For internal bores without rotation, Klemp et al. (1997) extended the work
of Rottman and Simpson (1989) to develop an improved phase speed relationship for internal
240 bores within the shallow water system that agrees very well with observations. Estimates of four
parameters are needed: the pre- and post-disturbance height as well an estimate of the reduced
242 gravity, which requires two potential temperature values. For S2 the 308 K (θ_2) isentrope is used
as the best estimate for the top of S2 (Fig. 4, top), which gives a pre-disturbance height (H_1) of
244 1500 m and a post-disturbance height (H_2) of 1750 m. The mass-weighted potential temperature
of the layer below θ_2 is 304.1 K (θ_1). These values and uncertainty estimates are summarized in
246 Table 1. Uncertainty estimates for θ_1 and θ_2 are simply $\pm 0.5 \text{ K}$, while height estimates are
calculated by taking the mean of the pre and post-disturbance heights over a span of 2 hours for

248 the isentropes spanning the θ_1 and θ_2 uncertainty estimates. The standard deviation of the mean
height is used as the uncertainty estimate. The phase speed of an internal bore is (Klemp et al.
250 1997):

$$C_B = [g' 2H_2^2 / (H_1 + H_2)]^{1/2} \quad (1)$$

252 Where g' is reduced gravity given by:

$$g' = g[(\theta_2 - \theta_1) / \theta_2] \quad (2)$$

254 The theoretical phase speed if S2 is an internal bore is: $C_B \approx 15.3 \pm 1.6 \text{ m s}^{-1}$. The uncertainty for
the theoretical phase speeds is the range using the fastest and slowest combination of parameter
256 values in Table 1. The model estimated phase speed of S2 is slightly faster than that of an
internal bore, but is within the uncertainty bounds and agrees the best with all possible dynamical
258 options for the phenomenon. Knupp (2006) observes a gravity current through the generation of
a leading internal bore to the dissipation of the gravity current and remaining solitary wave. This
260 evolution is very similar to that of S2, which is generated by a gravity current, transitions to a
mature bore with a dissipating gravity current and finally dissipates hours after the dissipation of
262 the generating gravity current (Fig. 4). However, an internal bore without rotation does not
explain the maximum perturbation heights and velocities near the coast as is simulated (Fig. 5).
264 Therefore, the dynamics of an internal bore without rotation does not fully explain the features of
S2.

266 Finally, the salient dynamics of the disturbance may be explained by an internal bore
under the influence of background rotation, or Kelvin shocks (Helfrich et al. 1999). Helfrich et
268 al. (1999) examine the nonlinear dynamics of Kelvin shocks and show that the largest
perturbation heights and along coast velocities are at the coast (in agreement with simulated S2,
270 cf. Fig. 5). They also show that as geostrophic adjustment begins to take place, non-zero across-

coast velocities are present. Assuming our disturbance can be considered a Kelvin shock, the
272 estimated phase speed of S2 would be (using a non-dimensional channel width $w \approx 1-2$,
appropriate for the GoC, and initial downstream fluid depth $d_o \approx 0.85$ of the upstream depth
274 (behind shock), their Fig. 21) $14.8 \pm 1.6 \text{ m s}^{-1}$, which is close to the modeled phase speed of 16.1
 m s^{-1} . With respect to the intensity of the Kelvin shock, the structure of the overlying
276 atmosphere as measured by the Scorer parameter is relevant (Crook 1986). The Scorer
parameter is a measure of the ability of the atmosphere to trap upward propagating wave energy
278 (Scorer 1949). It includes two terms, a term related to static stability and a term related to wind
profile curvature. If the Scorer parameter is larger than the square of the horizontal wavenumber
280 (k^2), upward propagation occurs. For S2, the Scorer parameter is nearly constant with height,
around $1.0 \times 10^{-6} \text{ m}^{-2}$ (Fig. 6), which is larger than waves with horizontal wavelengths $> 9 \text{ km}$.
282 Hence, vertical trapping of the disturbance is possibly minimal via the theory of Scorer (1949)
and simulations of bore type disturbances in Crook (1986). In the simulation, S2 loses amplitude
284 with time (Fig. 4) agreeing with the theoretical evolution of an internal bore. Including the
simulated features indicating rotational impacts and phase speed agreement the Kelvin shock
286 most completely describes the dynamics of S2.

288 *b. Gulf Surge*

1) INITIATION PHASE

290 The surge feature on 13 July is very complex with many subtle features. Initially, an
increase in flow from convectively cooled air associated with the outer bands of TS Blas near the
292 mouth of the GoC enhances the climatological cool dome over the southern GoC after the
passage of S2. Figure 7 displays a CS along AC2 at 0000 UTC 12 July, 0000 UTC and 0500

294 UTC 13 July, showing the buildup of the cool dome and encroachment of Pacific air into the
GoC which impinges upon the cool inflow from the mouth of the GoC in this case (NJ2012). In
296 response to this cool dome build up, surface pressure rises occur at LM between 0100-0600 UTC
(not shown) and the surge begins to propagate northward (NJ2012).

298 To estimate the modeled total speed of the surge between LM and Bahia Kino (BK), four
different criteria were used. First, the movement of the 2-D centroid of the 950-hPa moisture
300 flux maximum was estimated between 0500-0900 UTC. The time difference of maximum
moisture flux, maximum wind centroid, and maximum MSLP associated with the surge at LM
302 and BK were used as the second through fourth criteria respectively. These criteria give a model
total surge speed between LM and BK of $22.2 \pm 0.8 \text{ m s}^{-1}$. Using a corresponding estimate
304 along-surge flow in the preceding environment of $4.1 \pm 1.5 \text{ m s}^{-1}$ at BK, the modeled surge phase
speed is $18.1 \pm 1.7 \text{ m s}^{-1}$. Around and after 0500 UTC 13 July, substantial convective outflow
306 enters the western coastal plain of Mexico and adjacent GoC along the southern and central GoC
as the formative surge feature begins to propagate northward (Fig. 8, NJ2012). These outflow
308 impingements on the formative surge produce discrete propagation in its formative stages by
generating a new leading edge to the surge by 0700 UTC (Fig. 8) and are not accounted for by
310 any of the theory discussed herein.

At BK, there are multiple features on 13 July of which the gulf surge is the last. Briefly,
312 the first feature (0000 UTC 13 July) coinciding with an MSLP anomaly increase, temperature
decrease (Fig. 9) and wind shift is associated with the simulated sea breeze front moving over
314 BK. The increased wind anomaly around 0600-0800 UTC can be tied to a convective cluster
along the central SMO. During passage of it over BK, there is an increase in wind anomaly to
316 around 3 m s^{-1} along with a minimal MSLP rise, upward vertical velocities on the leading edge

and slight cooling above the surface (Fig. 9). These characteristics suggest this is an internal
318 bore that passes BK (Haertel et al. 2001; Knupp 2006; Martin and Johnson 2008).

The surge begins to pass over BK around 0830-0900 UTC (Fig. 9, NJ2012). It is
320 accompanied by a wind speed increase, cooling through a deeper layer and an anomalous surface
pressure increase (Fig. 9) all in phase with each other. Upward vertical velocities are also
322 present at the leading edge of the positive wind and negative temperature anomalies (Fig. 9).
The top of the surge at BK is estimated to be 308 K (~1500 m) using the vertical extent of
324 significant wind anomalies, cooling and moistening with the surge (Figs. 9 and 10 (at 1100
UTC)), which is also near the top of the SMO. Again the lowest 200 hPa of the atmosphere is
326 continuously stratified with no clear mixed and inversion layer present (Figs. 10 and 11) and has
a mean Brunt–Väisälä frequency of $\sim 0.01 \text{ s}^{-1}$. The surge winds are maximized near and inland of
328 the coast with isentropes that intersect the land and slope toward the surface moving away from
the SMO, relevant to CTDs of any type. Finally, the wind and MSLP anomalies associated with
330 the surge occur for approximately 5 hours (Fig. 9), implying an estimated wavelength of ~ 650
km.

332 As with S2, the generation mechanism, large phase speed and short wavelength rule out
topographically trapped Rossby waves as the dynamical mechanism for the surge and will not be
334 discussed further. Gravity currents are integral in the development of the initial surge, and
would generate in phase positive wind, pressure and negative temperature anomalies. The
336 estimated maximum phase speed of a gravity current at BK is $\sim 17 \text{ m s}^{-1}$ using a $\Delta\theta$ of 3 K and a
cold pool height of 1500 m. However, the anomalous surface cooling is rather weak and occurs
338 several hours after the initial passage of the surge over BK. Also the maximum wind and most

negative temperature anomalies are centered above the surface. These factors suggest that the
340 phenomenon is not a gravity current.

Multiple factors argue against a Kelvin wave interpretation. Stratification without a clear
342 inversion layer precludes inversion-trapped Kelvin waves while linear step-trapped Kelvin waves
would have a phase speed of $\sim 9 \text{ m s}^{-1}$, half that of the modeled surge. The surge at BK is likely
344 not sub-inertial, with an angular frequency of $\omega_s \approx 1.4 \times 10^{-4}$, larger than Corilois at 30° N ($7.3 \times$
 10^{-5} s^{-1}). Additionally, there are non-negligible across-coast velocities within the surge (Fig.
346 11).

The above considerations lead to the conclusion that the surge at this stage can best be
348 explained in terms of bore dynamics. The theoretical phase speed of an internal bore at BK is C_B
 $\approx 13.2 \pm 4.8 \text{ m s}^{-1}$ while that of a Kelvin shock is $\sim 12.8 \pm 4.8 \text{ m s}^{-1}$ (Tables 1, 2). These phase
350 speeds are about 5 m s^{-1} slower than that of the modeled surge, likely due to discrete propagation
of the surge in its formative stages. As noted above and in NJ2012, multiple convective outflows
352 impinge on the southern and central GoC between 0500-0800 UTC. These outflows generate a
new leading edge to the surge by 0700 UTC (Fig. 8), which impacts the total system speed in a
354 way that is not accounted for by the theory used herein. Overall, the Kelvin shock is the best
dynamical fit for the surge at BK; it can account for the generation mechanism, wind maximum,
356 potential temperature slope and across-coast flow. Focus will now shift to the mature phase of
the surge as simulated between Bahia Kino (BK) and Puerto Penasco (PP).

358

2) MATURE PHASE

360 As at BK, more than one feature passes over PP. The first two features are generated by
convective outflow from two convective clusters along the northern SMO (NJ2012). A weak

362 feature passage, consistent with that of a gravity current (Simpson 1997; Haertel et al. 2001), is
modeled with an MSLP rise beginning around 0100 UTC, an associated wind speed increase by
364 0200 UTC, low-level and surface cooling and an MSLP rise (Fig. 12) and is the first of three
distinct feature passages at PP. The second feature passes over PP from 0500-0800 UTC and has
366 cooling centered around 975 hPa, a MSLP anomaly rise between 0600 and 0830 UTC, and the
initial wind anomaly increase occurs near 975 hPa (Fig. 12, 0830 UTC). These characteristics
368 are consistent with the passage of an internal bore (Haertel et al. 2001; Knupp 2006; Martin and
Johnson 2008).

370 There is a small break period after the 0500-0800 UTC bore passage noted by the
decrease in the wind and MSLP anomaly just before 0900 UTC (Fig. 12) before the surge feature
372 begins to impact PP. After 0900 UTC a more significant increase in the near surface negative
temperature anomalies is visible through ~1800 UTC, centered at 975-950 hPa with a maximum
374 after ~1200 UTC (Fig. 12). This feature is the modeled surge passing over PP. The surge is
associated with in phase positive wind and MSLP anomalies and negative temperature anomalies
376 that slightly lag. There are also several regions of upward motion throughout the surge (Fig. 12).
Surge cross sections AC3 and AG2 highlight across-coast flow (Fig. 13), isentropes that intersect
378 the terrain (Fig. 13) and slope downward away from the SMO, and maximum wind anomalies
co-located with the most negative temperature anomalies (Fig. 14). Also, there is a distinct
380 transition to more positive along CS winds (southeasterly meteorological winds) and more
negative temperature anomalies, both of which are maximized around 975-950 hPa and deepen
382 behind the leading edge of the surge as it approaches PP (Fig. 14). Between BK and PP (320
km), the movement of the modeled surge was estimated using the same four criteria as between
384 LM and BK. These criteria give an estimated total surge speed of $20.4 \pm 1.4 \text{ m s}^{-1}$ between BK

and PP. The along surge flow is estimated at $7 \pm 1.5 \text{ m s}^{-1}$, resulting in a modeled surge phase
386 speed of $13.4 \pm 2.1 \text{ m s}^{-1}$. The positive southerly wind anomalies occur for ~10-12 hours at PP
(Fig. 12) giving an estimated wavelength of ~1100 km and an angular frequency of $\omega_s \approx 7.7 \times 10^{-5}$
388 s^{-1} .

The lack of strong surface cooling and positive wind anomalies exclude gravity currents
390 as the likely dynamical mechanism for the surge in the northern GoC, although they may play a
role in amplifying the overall disturbance. Also, coastally trapped Kelvin waves can be
392 disqualified as the dynamical mechanism. Assuming a surge top of 308.5 K (Table 1), linear
shallow water Kelvin waves trapped by an inversion layer would have a phase speed of 7.8 ± 1.2
394 m s^{-1} , while step-trapped Kelvin waves would have a phase speed of ~8-9 m s^{-1} again. These
speeds are 4-5 m s^{-1} slower than modeled and outside the uncertainty bounds. Also, the surge at
396 PP may not be sub-inertial ($\omega_s \approx 7.7 \times 10^{-5}$, $f \approx 7.3 \times 10^{-5}$ at 30° N) and there is a net northward
moisture transport to the northern GoC (NJ2012), which is not possible with linear Kelvin waves
398 (Zehnder 2004). Finally, non-linear Kelvin waves would have a phase speed only slightly slower
than modeled (~12 m s^{-1} for shallow water type Kelvin waves Ralph et al. 2000), however the
400 extent of across-coast flow present (Fig. 13) is not accounted for by coastally trapped Kelvin
wave theory (Reason and Steyn 1992).

402 Kelvin shocks or internal bores modified by rotation are the best dynamical match for the
surge in the northern GoC. The phase speed for an internal bore at PP is $C_B \approx 13.6 \pm 2.4 \text{ m s}^{-1}$
404 and a Kelvin shock is $\sim 13.2 \pm 2.4 \text{ m s}^{-1}$ (Table 2). Including the along surge flow results in total
speeds of $20.2\text{-}20.6 \pm 2.4 \text{ m s}^{-1}$, corresponding very well with the modeled surge total speed.
406 The Kelvin shock solution also explains the intersecting isentropes along the SMO and the decay
away from the SMO, the wind maximum near the coast and can account for some of the across-

408 coast flow modeled. Interestingly, the estimated phase speed for an internal bore at BK agrees
with the modeled phase speed estimate between BK and PP as well. This suggests the surge has
410 fully developed by BK and is one dynamical feature throughout the central and northern GoC.

Finally, on 13 July the Scorer parameter has two areas of distinct decrease with height, -
412 0.75-1.5 km and .2-3.2 km (Fig. 6). The lower layer is related to the GoC low-level jet and the
top of the boundary layer, while the second layer has coincident areas of decreasing stability and
414 increasing wind curvature with height, which implies that the environment on 13 July is
conducive to gravity wave trapping or internal bores (Crook 1986). An environment suitable for
416 internal bore propagation on 13 July and not 12 July explains the inability of S2 to propagate into
the northern GoC and its loss of amplitude with northward extent. The surge on 13 July is able
418 to maintain its amplitude and intensity while traveling over 300 km due to the favorable
environment for bore propagation without energy loss (Crook 1986).

420 One complicating factor in this analysis is that at the northern end of the gulf, the
topography fans out tremendously and becomes less continuous (Fig. 2), which could explain the
422 extensive cross-coast flow. In this region, the arguments regarding coastally trapped
disturbances are more tenuous. Reason and Styen (1992) include dissipation due to gaps in
424 topography. Gaps in the coastal barrier are parameterized via a small across-coast flow
component. However, gently sloping terrain with gaps as is seen in the northern GoC (Figs. 2,
426 11 and 13) is not accounted for by any theory. The sloping topography may allow for across-
coast flow via incomplete blocking of the surge event. In any event, the Kelvin shock most
428 favorably accounts for the features of the surge in the northern GoC. Non-ideal terrain may then
account for the increased across-coast flow.

430
c. Comparison of modeled to observed surge

432 The general features of the modeled precursor wave and surge agree qualitatively well
with the observed as reported in NJ2012. A convectively generated gravity current initiates the
434 precursor Kelvin shock on 12 July in both the observations and model. Multiple convective
clusters in the southern GoC on early 13 July generate various convective outflows that interact
436 with the formative surge over the southern GoC as observed (NJ2012), indicating the model
simulation captures the dynamics of surge initiation. While the theoretical phase and total
438 system speeds increase between BK and PP (Table 2), the modeled surge speed decreases from
 $22.4 \pm 0.8 \text{ m s}^{-1}$ to $20.4 \pm 1.4 \text{ m s}^{-1}$ between the LM-BK and BK-PP legs, which is in general
440 agreement with observations (RJ2007). The pre-surge and surge features at BK, a stronger surge
feature at PP, and a slight lag in moisture flux increases at BK and PP are all present in RJ2007.
442 The height of the surge top decreases about 400 m with northward extent, which is also in
agreement with observations.

444 As discussed in NJ2012 the depth of the high winds and largest cooling associated with
the modeled surge are too shallow. However, when examining Fig. 12 of RJ2007, the top of the
446 inversion is at a similar height ($\sim 900 \text{ hPa}$) and temperature (309 K) to that of the modeled surge.
The wind field in RJ2007 is much stronger throughout the troposphere over the course of the
448 observed surge event, suggesting the model is not capturing some other process(es) (e.g., the
modeled maximum large scale MSLP pressure gradient between LM and PP is 2.4 hPa less than
450 observed). The core of the modeled surge near PP is at roughly 950 hPa, which does agree well
with the observed surge. However, there is modeled wind bias (model – obs) of almost -4 m s^{-1}
452 between 0800-1800 UTC 13 July, during the core time of the surge event. Addition of that bias
to the modeled wind field would give the appearance of a much deeper surge event, in better
454 agreement with the observations. The similarity of the modeled surge to that observed including

the model wind bias provides further evidence that a Kelvin shock can explain both the modeled
456 and observed surge on 13 July 2004.

458 **4. Summary**

A high-resolution simulation of a gulf surge event during the North American Monsoon
460 Experiment is examined herein to determine the dynamical evolution of the surge feature. The
simulation provides a good representation of the features of the surge event (NJ2012).
462 Comparisons to the theoretical characteristics of topographically trapped Rossby waves, gravity
currents, Kelvin waves and internal bores are made to diagnose the dynamical mechanisms of the
464 precursor wave and the surge event. Overall, the entire event is complex with many subtle
features and convective episodes.

466 *a. Simulated surge description*

Initially, convection associated with the tropical easterly wave (TEW) precursor to
468 tropical storm (TC) Blas creates a convective cluster in the southern Gulf of California (GoC) on
12 July around 0600-0900 UTC. This cluster interacts with the climatological cool dome to
470 create an internal bore which propagates up the GoC, slowly moves ahead of the dissipating
gravity current and becomes diffuse just south of Bahia Kino (BK) around 2200 UTC 12 July
472 (feature labeled S2 in the text). Southerly flow, moistening and slight cooling below are present
in the simulation behind the wave. Convection then forms along the length of the Sierra Madre
474 Occidental (SMO) late on 12 July into 13 July. Inflow from the mouth of the GoC and Pacific
Ocean along with convective outflow impinging on the southern GoC initiates the surge feature
476 by early on 13 July. Continued convective outflow entering the GoC intensifies the surge as it
propagates up the GoC. As the core of the surge passes through BK and Puerto Penasco (PP), it

478 is most likely an internal bore influenced by the earth's rotation or a *Kelvin shock* after Helfrich
et al. (1999). Substantial low-level cooling and moistening are associated with the simulated
480 surge feature as observed.

That the surge signal seen at PP on 13 July is preceded by a wave on 12 July associated
482 with a TEW could possibly explain how TEW/TCs are tied to gulf surge events. Stensrud et al.
(1997), Fuller and Stensrud (2000) and Adams and Stensrud (2007) show that gulf surges are
484 typically preceded by TEW passage. Adams and Stensrud (2007) also find that removal of
TEWs in a simulation results in weaker surges that occur at different times and are often
486 associated with waves generated internally by the model. In this case, removal of the bore on 12
July may change the evolution and character of the surge event on 13 July since it is followed by
488 cooling, moistening and southerly flow in the southern and central GoC that extends into 13 July.
It could be that without this initial cooling and inflow into the southern GoC, the surge and
490 convective initiation and evolution along the southern SMO would be different. This should be
the subject of further study.

492

b. Surge dynamics

494 The features associated with the disturbance on 12 July (labeled S2) indicate that it is an
internal bore/Kelvin shock that moves ahead of the dissipating initiating gravity current (S1)
496 with minimal surface cooling, non-zero across-coast flow, isentropes that intersect the SMO, and
maximum winds and lowest potential temperatures near the coastline. S2 decays with time as it
498 move along the GoC, washing out just south of BK around 2000-2200 UTC. The vertical profile
of the Scorer parameter just ahead of S2 (Fig. 6) shows no trapping layer above indicating that
500 the modeled decay is at least partially due to vertical energy loss.

On 13 July the initial surge forms through a consolidation of cool air moving into the
502 GoC from near the mouth, along with convective outflows from the west slopes of the SMO
impinging on the coastal plain around 0500 UTC 13 July. As the surge moves up the GoC, many
504 convective outflows, either gravity currents or bores, impinge upon the GoC near and ahead of
the initial Kelvin wave, causing enhancement and deepening of the cool anomaly. The surge
506 begins to impact BK around 0830 UTC 13 July (Fig. 9). The modeled surge has a total system
speed of $\sim 22 \text{ m s}^{-1}$ in the southern and central GoC, which is faster than all theoretical estimates
508 for the surge at BK ($\sim 17 \text{ m s}^{-1}$ for a Kelvin shock, Table 2). This is due to the impinging
outflows creating a new surge leading edge around 0700 UTC in the central GoC, increasing the
510 surge system speed between LM and BK in a way not accounted for by the steady propagation
used in the formulation of phase speeds for Kelvin shocks (Helfrich et al. 1999).

512 At PP the gulf surge is preceded by two weak features, both generated by convective
clusters decaying along the northern SMO. When the surge reaches PP it has a modeled total
514 system speed of $20.4 \text{ m s}^{-1} \pm 1.4 \text{ m s}^{-1}$. The theoretical phase speed estimate for a Kelvin shock
is $13.2 \pm 2.4 \text{ m s}^{-1}$ and $13.4 \pm 2.1 \text{ m s}^{-1}$ for the observed surge (Table 2). This, along with the
516 modeled features of maximum above surface cooling, a positive MSLP anomaly, isentropes that
intersect the SMO and decay toward the surface away from the SMO, maximum wind velocities
518 near the coast, and non-zero across-coast flow support the argument that the modeled surge at PP
is a Kelvin shock, or an internal bore modified by rotation and bounded on the right by the SMO.

520

Acknowledgements. The authors would like to thank Paul Ciesielski, Brian McNoldy, and Rick
522 Taft for their assistance relating to this research. The authors would also like to thank two
anonymous reviewers and Editor Dale Durran for greatly improving this manuscript. This work

524 was supported by NASA Headquarters through NASA grants “NNX07AD35G” and
“NNX10AG81G”, and by the National Science Foundation, by both the Mesoscale Dynamic
526 Meteorology Program, under grant ATM-0639461, and the Physical and Dynamic Meteorology
Program, under grant AGS-0966758. Finally, we would like to acknowledge high-performance
528 computing support provided by NCAR's Computational and Information Systems Laboratory,
sponsored by the National Science Foundation.

530

References

- 532 Adams, J. L., and D. J. Stensrud, 2007: Impact of tropical easterly waves on the North American
monsoon. *J. Climate*, **20**, 1219-1238.
- 534 Anderson, B. T., J. O. Roads, and S.-C. Chen, 2000a: Large-scale forcing of summertime
monsoon surges over the Gulf of California and the southwestern United States. *J.*
536 *Geophys. Res.*, **105**, 24 455- 24 467.
- Anderson, B. T., J. O. Roads, and S.-C. Chen, 2000b: Regional simulation of the low-level
538 monsoon winds over the Gulf of California and southwestern United States. *J. Geophys.*
Res., **105**, 17 955-17 969.
- 540 Benjamin, T. B., 1968: Gravity currents and related phenomena. *J. Fluid. Mech.*, **31**, 209-248.
- Berbery, E. H., 2001: Mesoscale moisture analysis of the North American Monsoon. *J. Climate*,
542 **14**, 121-137.
- Bordoni, S., and B. Stevens, 2006: Principal component analysis of the summertime winds over
544 the Gulf of California: A gulf surge index. *Mon. Wea. Rev.*, **134**, 3395-3414.
- Brenner, I. S., 1974: A surge of maritime tropical air-Gulf of California to the southwestern
546 United States. *Mon. Wea. Rev.*, **102**, 375-389.
- Bruyere, C., M. Duda, J. Dudhia, D. Gill, H.-C. Lin, J. Michalakes, S. Rizvi, W. Wang, and X.
548 Zhang, 2010: Weather Research and Forecasting ARW Version 3 Modeling System
User's Guide, Mesoscale & Microscale Meteorology Division, National Center for
550 Atmospheric Research, 312 pp. [Available from the National Center for Atmospheric
Research, Boulder, CO 80301.
- 552 Bryan, G. H. and H. Morrison, 2012: Sensitivity of a simulated squall line to horizontal
resolution and parameterization of microphysics. *Mon. Wea. Rev.*, **140**, 202-225.

- 554 Crook, N. A., 1986: The effect of ambient stratification and moisture on the motion of
atmospheric undular bores. *J. Atmos. Sci.*, **43**, 171-181.
- 556 Dorman, C., 1985: Evidence of Kelvin waves in California's marine layer and related eddy
generation. *Mon. Wea. Rev.*, **113**, 827-839.
- 558 Dorman, C., 1987: Possible role of gravity currents in northern California's coastal summer wind
reversals. *J. Geophys. Res.*, **92**, 1497-1506.
- 560 Douglas, M. W., and J. C. Leal, 2003: Summertime surges over the Gulf of California: Aspects
of their climatology, mean structure, and evolution from radiosonde, NCEP reanalysis,
562 and rainfall data. *Wea. Forecasting*, **18**, 55-74.
- Durran, D. R., 2000: Small-amplitude coastally trapped disturbances and the reduced-gravity
564 shallow-water approximation. *Quart. J. Roy. Meteor. Soc.*, **126**, 2671-2689.
- Federov, A. V., and W. K. Melville, 1996: Hydraulic jumps at boundaries in rotating fluids. *J.*
566 *Fluid Mech.*, **324**, 55-82, doi:10.1017/S0022112096007835.
- Fuller, R. D., and D. J. Stensrud, 2000: The relationship between tropical easterly waves and
568 surges over the Gulf of California during the North American monsoon. *Mon. Wea. Rev.*,
128, 2983-2989.
- 570 Gill, A. E., 1977: Coastally trapped waves in the atmosphere. *Quart. J. Roy. Meteor. Soc.*, **103**,
431-440.
- 572 Gill, A. E., 1982: Atmosphere-Ocean Dynamics. Academic Press, 662 pp.
- Gochis, D. J., A. J. Jimenez, C. J. Watts, J. Garatuza-Payan, and W. J. Shuttleworth, 2004:
574 Analysis of 2002 and 2003 warm season precipitation from the North American Monsoon
Experiment event rain gauge network. *Mon. Wea. Rev.*, **132**, 2938-2953.

- 576 Haertel, P. T., R. H. Johnson, and S. N. Tulich, 2001: Some simple simulations of thunderstorm outflows. *J. Atmos. Sci.*, **58**, 504-516.
- 578 Hales, J. E., Jr., 1972: Surges of maritime tropical air northward over the Gulf of California. *Mon. Wea. Rev.*, **100**, 298-306.
- 580 Helfrich, K. R., A. C. Kuo, and L. J. Pratt, 1999: Nonlinear Rossby adjustment in a channel. *J. Fluid Mech.*, **390**, 187-222, doi:10.1017/S0022112099005042.
- 582 Higgins, R. W., W. Shi, and C. Hain, 2004: Relationships between Gulf of California moisture surges and precipitation in the southwestern United States. *J. Climate*, **17**, 2983-2997.
- 584 Higgins, R. W., and W. Shi, 2005: Relationships between Gulf of California moisture surges and tropical cyclones in the eastern Pacific basin. *J. Climate*, **18**, 4601-4620.
- 586 Higgins, R. W., and Coauthors, 2006: The North American Monsoon Experiment (NAME) 2004 field campaign and modeling strategy. *Bull. Amer. Meteor. Soc.*, **87**, 70-94.
- 588 Holland, G. J. and L. M. Leslie, 1986: Ducted coastal ridging over S.E. Australia. *Quart. J. Roy. Meteor. Soc.*, **112**, 731-748
- 590 Klemp, J. B., R. Rotunno, and W. C. Skamarock, 1997: On the propagation of internal bores. *J. Fluid Mech.*, **331**, 81-106.
- 592 Knupp, K., 2006: Observational analysis of a gust front to bore to solitary wave transition within an evolving nocturnal boundary layer. *J. Atmos. Sci.*, **63**, 2016-2035.
- 594 Maddox, R. A., D. M. McCollum, and K. W. Howard, 1995: Large-scale patterns associated with severe summertime thunderstorms over central Arizona. *Wea. Forecasting*, **10**, 763-778.
- 596 Maloney, E. D., and D. L. Hartmann, 2000: Modulation of eastern North Pacific hurricanes by the Madden-Julian oscillation. *J. Climate*, **13**, 1451-1460.

598 Martin, E. R., and R. H. Johnson, 2008: An observational and modeling study of an atmospheric
internal bore during NAME 2004. *Mon. Wea. Rev.*, **136**, 4150-4167.

600 Mass, C. F., and M. D. Albright, 1987: Coastal southerlies and along-shore surges of the west
coast of North America: Evidence of mesoscale topographically trapped response to
602 synoptic forcing. *Mon. Wea. Rev.*, **115**, 1707-1738.

Mejia, J. F., M. W. Douglas, and P. J. Lamb, 2010: Aircraft observations of the 12-15 July 2004
604 moisture surge event during the North American Monsoon Experiment. *Mon. Wea. Rev.*,
138, 3498-3513.

606 Mesinger, F. and co-authors, 2006: North American regional reanalysis. *Bull. Amer. Meteor.
Soc.*, **87**, 343-360.

608 Newman, A., and R. H. Johnson, 2012: Simulation of a North American monsoon gulf surge
event and comparison to observations. *Mon. Wea. Rev.*, **140**, 2534-2554.

610 Ralph, F. M., P. J. Neiman, P. O. G. Persson, J. M. Bane, M. L. Cancillo, J. M. Wilczak, and W.
Nuss, 2000: Kelvin waves and internal bores in the marine boundary layer inversion and
612 their relationship to coastally trapped wind reversals. *Mon. Wea. Rev.*, **128**, 283-300.

Reason, C. J. C., and D. G. Steyn, 1992: The Dynamics of Coastally Trapped Ridges in the
614 Lower Atmosphere. *J. Atmos. Sci.*, **49**, 1677-1692.

Rogers, P. J., and R. H. Johnson, 2007: Analysis of the 13-14 July gulf surge event during the
616 2004 North American Monsoon Experiment, *Mon. Wea. Rev.*, **135**, 3098-3117.

Rogerson, A. M., and R. M. Samelson, 1995: Synoptic forcing of coastal-trapped disturbances in
618 the marine atmospheric boundary layer. *J. Atmos. Sci.*, **52**, 2025-2040.

Rottman, J. W., and J. E. Simpson, 1989: The Formation of Internal Bores in the Atmosphere: A
620 Laboratory Model. *Quart. J. Roy. Meteor. Soc.*, **115**, 941-963.

- 622 Scorer, R. S., 1949: Theory of waves in the lee of mountains. *Quart. J. Roy. Meteor. Soc.*, **75**,
41-56.
- 624 Simpson, J. E., 1997: Gravity currents in the environment and the laboratory. Cambridge
University Press, 244 pp.
- 626 Skamarock, W. C., R. Rotunno, and J. B. Klemp, 1999: Models of Coastally Trapped
Disturbances. *J. Atmos. Sci.*, **56**, 3350-3365.
- 628 Stensrud, D. J., R. L. Gall, and M. K. Nordquist, 1997: Surges over the Gulf of California during
the Mexican monsoon. *Mon. Wea. Rev.*, **125**, 417-437.
- 630 Sukoriansky, S., B. Galperin, and V. Perov, 2006: A quasi-normal scale elimination model of
turbulence and its application to stably stratified flows. *Nonlinear Processes in Geophys.*,
17,
- 632 Thompson, G., P. R. Field, R. M. Rasmussen, and W. D. Hall, 2008: Explicit forecasts of winter
precipitation using an improved bulk microphysics scheme. Part II: Implementation of a
634 new snow parameterization. *Mon. Wea. Rev.*, **136**, 5095-5115.
- 636 Zehnder, J. A., 2004: Dynamic mechanisms of the Gulf surge. *J. Geophys. Res.*, **109**, D10107,
doi:10.1029/2004JD004616.

638 List of Figures:

Figure 1. Overview of North American Monsoon region during the 12-14 July 2004 surge event.

640 Geographic and political boundaries are noted. The black line indicates the general path of
tropical storm Blas, “heat low” indicates the position of surface heat low in desert southwest US,
642 while the Pacific surface high pressure center is indicated by H. Thunderstorm symbols indicate
general area of convection thought to initiate surge events in Stensrud et al. (1997).

644 Figure 2. Core NAM region with the model domain outlined (trapezoid). Also depicted are the

646 three ISS sites (large circles): Puerto Penasco (PP), Bahia Kino (BK) and Los Mochis (LM).

AG1, AG2, AC1, AC2, AC3, and AC4 denote the along-gulf and across-gulf cross-section

648 locations respectively.

650 Figure 3. Progression of the leading edge of S2 and the gulf surge in the simulation. Times
depicted are 1000, 1200, 1400, 1600, 1800, and 2000 UTC 12 July for S2 (dashed lines) and

652 0300, 0500, 0700, 0900, 1100, and 1300 UTC 13 July for the gulf surge (solid lines). The lines
progress from light to dark in chronological order.

654 Figure 4. Potential temperature (K, black lines), moisture flux ($\text{g m kg}^{-1} \text{ s}^{-1}$, shading) and coast

656 relative moisture flux vectors (arrows) at 1600 UTC (top) and 2000 UTC (bottom) 12 July 2004
along AG1. S1 denotes cold pool associated with convection near GoC entrance, S2 denotes

658 deeper disturbance discussed in Mejia et al. (2010). Red lines give general boundaries of S1 and
S2.

660

662 Figure 5. Simulated potential temperature (K, white contours), wind magnitude (m s^{-1} , shading) and coast relative wind vectors (arrows) along across-gulf cross section AC1 at 1730 UTC 12 July. Black shading indicates topography, while the red line indicates the coastline.

664 Figure 6. Vertical profile of the Scorer parameter at 1300 UTC 12 July ahead of S2 (solid gray line) and at 0600 UTC 13 July (black line) ahead of the surge.

668 Figure 7. Simulated potential temperature (K, white contours), wind magnitude (m s^{-1} , shading) and coast relative wind vectors (arrows) taken along across-gulf cross section AC2 at 0000 UTC 12 July (top), 0000 UTC (middle), and 0500 UTC 13 July (bottom). Black shading indicates topography, while the red line indicates the coastline.

672 Figure 8. 975 hPa moisture flux ($\text{g m kg}^{-1} \text{ s}^{-1}$) at 0500 (top) and 0700 (bottom) UTC 13 July. The red lines denote the approximate position of the surge leading edge.

676 Figure 9. Bahia Kino temperature anomalies (K, shading), wind anomalies (m s^{-1} , black contours), and vertical velocity (Pa s^{-1} , white contours: dashed upward, contour interval 0.5 Pa s^{-1}) in the top panel. Mean Sea Level Pressure (MSLP) anomalies (hPa) in the middle panel. 950 hPa wind speed (m s^{-1}) and direction anomalies (deg) in the bottom panel. All panels are anomalies compared to the diurnal mean for the WRF simulation period 0000 UTC 12 July to 0000 UTC 14 July and display 18 UTC 12 July – 00 UTC 14 July. Red vertical lines denote passage of sea breeze, minor bore, and gulf surge event in chronological order.

684 Figure 10. Potential temperature (K) (a) and mixing ratio (g kg^{-1}) (b) for the surge event at Bahia
Kino at 0300 (black), 0730 (med. gray) and 1100 (light gray) UTC 13 July.

686

Figure 11. Simulated potential temperature (K, white contours), wind magnitude (m s^{-1} , shading)
688 and coast relative wind vectors (arrows) taken along across-gulf cross section AC3 at 1000 UTC
13 July (top). Black shading indicates topography, while the red line indicates the coastline.

690

Figure 12. Puerto Penasco temperature anomalies (K, shading), wind anomalies (m s^{-1} , black
692 contours), and vertical velocity (Pa s^{-1} , white contours: dashed upward, contour interval 0.5 Pa s^{-1})
in the top panel. Mean Sea Level Pressure (MSLP) anomalies (hPa) in the middle panel. 950
694 hPa wind speed (m s^{-1}) and direction anomalies (deg) in the bottom panel. All panels are
anomalies compared to the diurnal mean for the WRF simulation period 0000 UTC 12 July to
696 0000 UTC 14 July and display 18 UTC 12 July – 00 UTC 14 July.

698 Figure 13. Simulated potential temperature (K, white contours), wind magnitude (m s^{-1} , shading)
and coast relative wind vectors (arrows) taken along across-gulf cross section AC4 at 1300 UTC
700 13 July (top). Black shading indicates topography, while the red line indicates the coastline.

702 Figure 14. Potential temperature differences (white contours) and along cross section wind
differences (arrows and shading) along AG2 on 13 July. Differences are taken as 1030 UTC –
704 0500 UTC (top panel), 1300 UTC – 0500 UTC (middle panel), 1430 – 0500 UTC (bottom
panel).

706

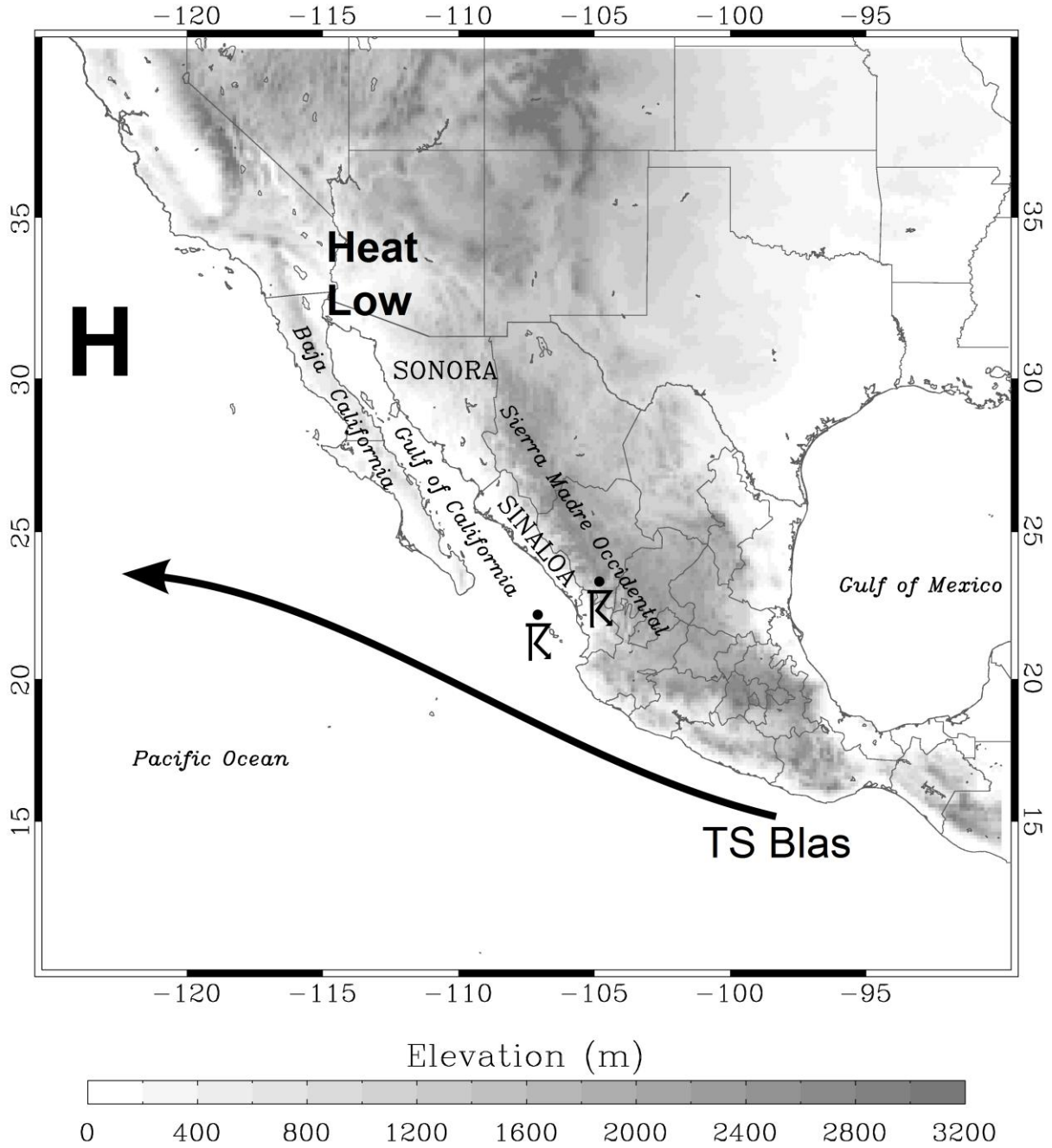
708 Table 1. Parameter and estimated uncertainty values for H_1 , H_2 , θ_1 , θ_2 in the simulation for the 12 July feature (S2) at Los Mochis and the surge at Bahia Kino (BK) and Puerto Penasco (PP).

	H_1	H_2	θ_1	θ_2
12 July (S2)	1500 ± 120 m	1750 ± 80 m	304.1 ± 0.2 K	308.0 ± 0.5 K
Surge at BK	950 ± 90 m	1430 ± 220 m	304.3 ± 0.2 K	307.5 ± 0.5 K
Surge at PP	470 ± 30 m	1030 ± 70 m	304.4 ± 0.5 K	308.5 ± 0.5 K

710 Table 2. Simulated and theoretical phase speeds and estimated uncertainty for the 12 July feature (S2) at Los Mochis and the surge at Bahia Kino (BK) and Puerto Penasco (PP).

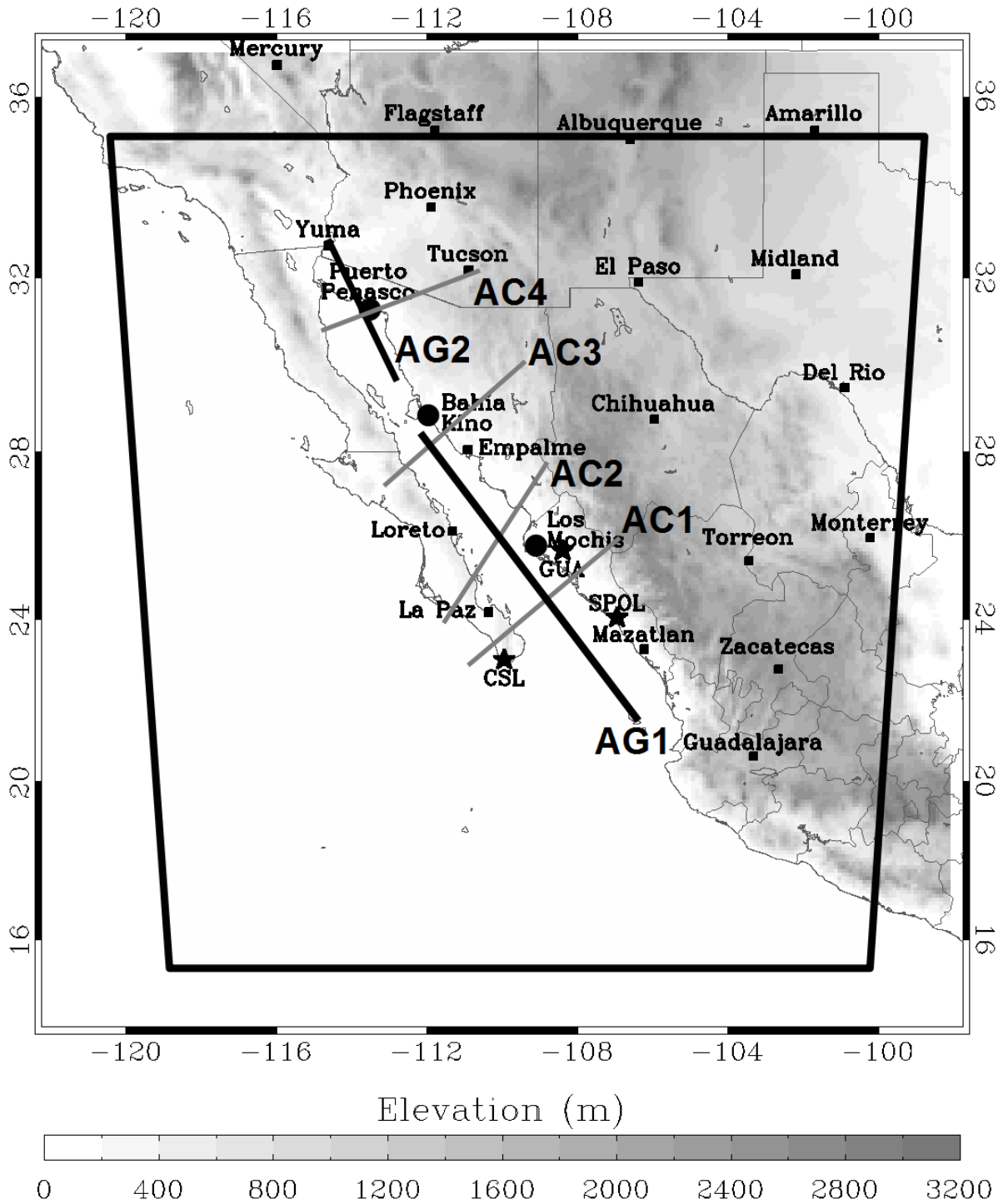
	C_{WRF}	C_{STKW}	C_{B}
12 July (S2)	$16.1 \pm 1.9 \text{ m s}^{-1}$	$8.5 \pm 1.5 \text{ m s}^{-1}$	$15.3 \pm 1.6 \text{ m s}^{-1}$
Surge at BK	$18.1 \pm 1.7 \text{ m s}^{-1}$	$8.5 \pm 1.5 \text{ m s}^{-1}$	$13.2 \pm 4.8 \text{ m s}^{-1}$
Surge at PP	$13.4 \pm 2.1 \text{ m s}^{-1}$	$8.5 \pm 1.5 \text{ m s}^{-1}$	$13.6 \pm 2.4 \text{ m s}^{-1}$

712

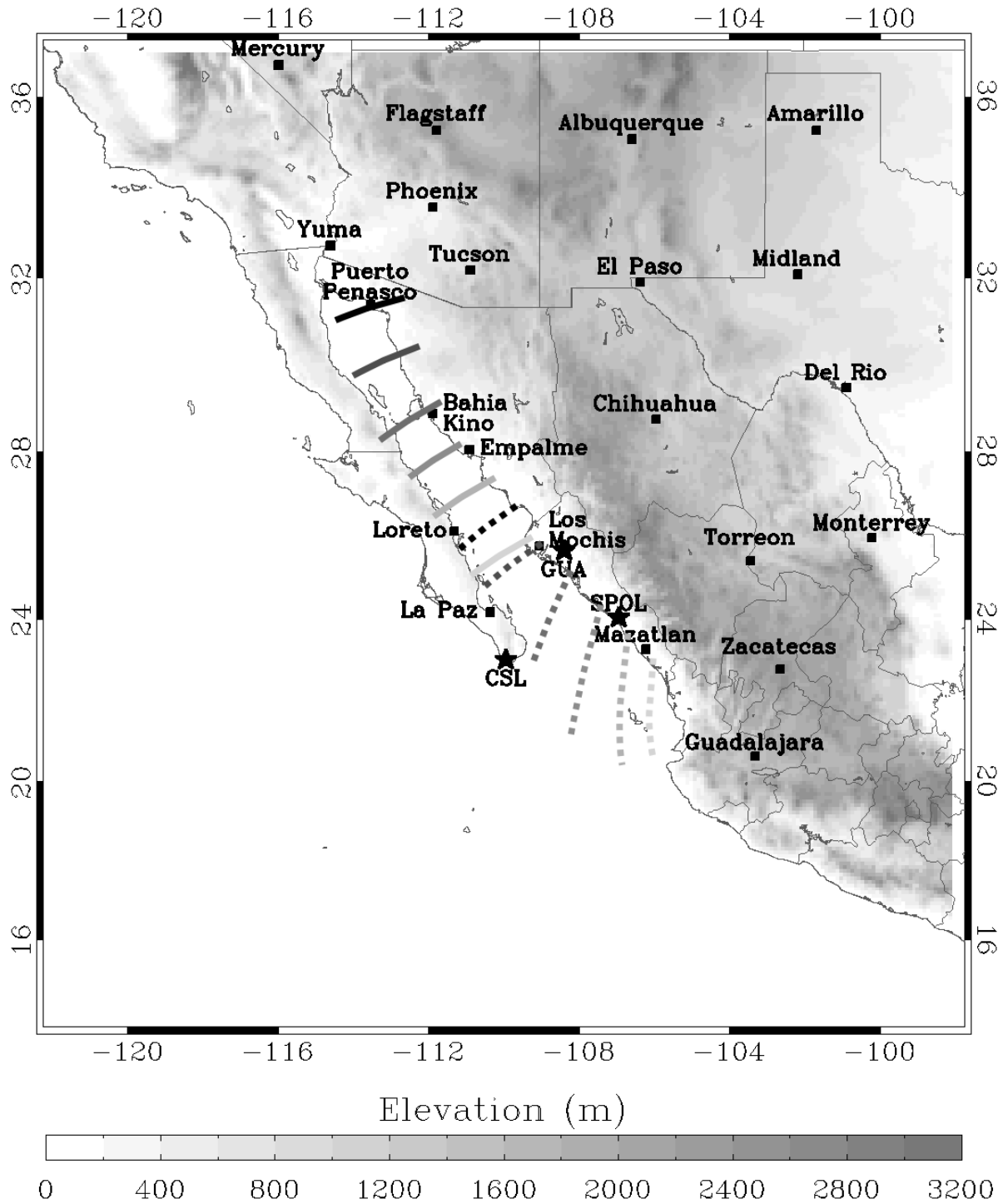


714

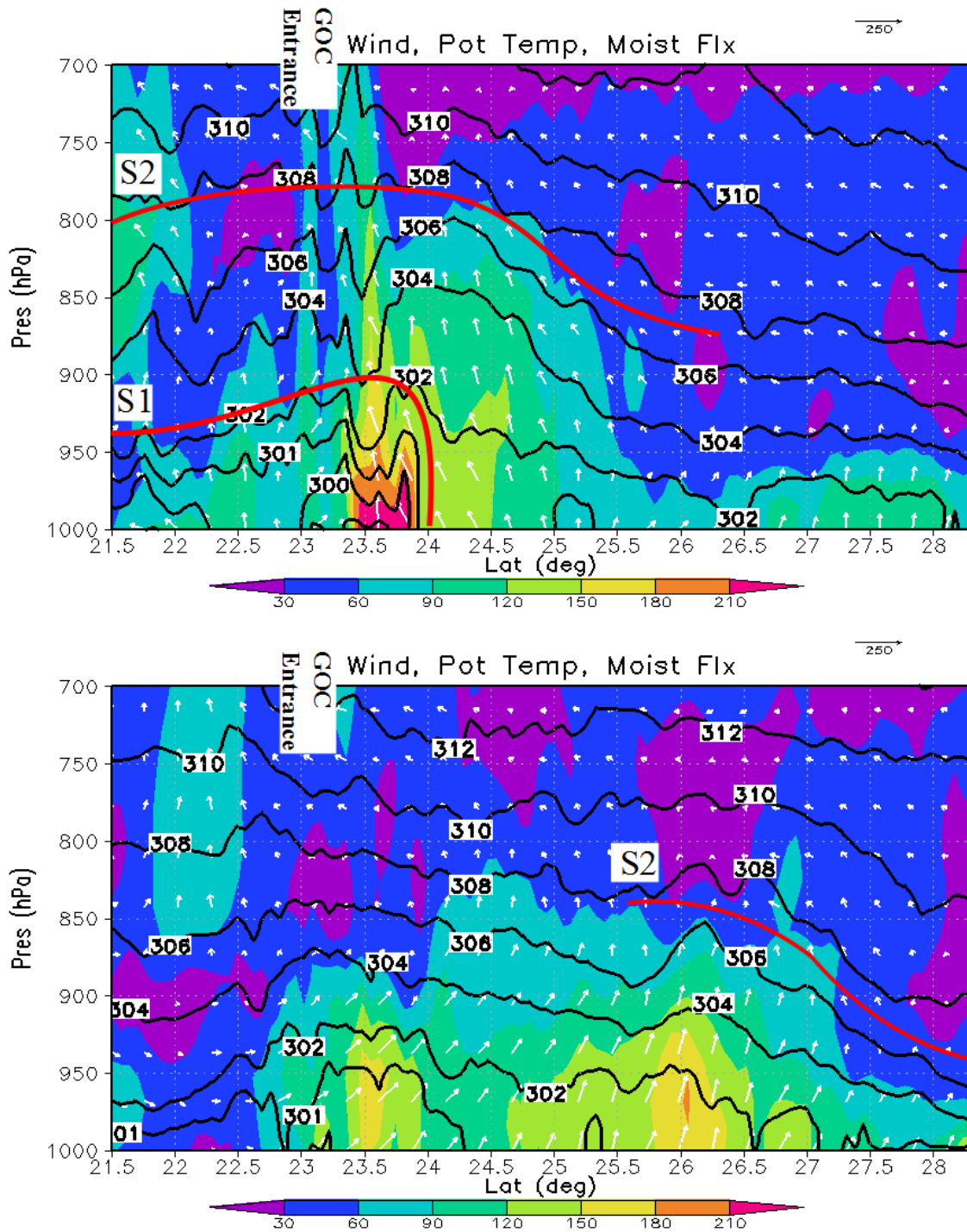
716 Figure 1. Overview of North American Monsoon region during the 12-14 July 2004 surge event.
 718 Geographic and political boundaries are noted. The black line indicates the general path of
 720 tropical storm Blas, “heat low” indicates the position of surface heat low in desert southwest US,
 while the Pacific surface high pressure center is indicated by H. Thunderstorm symbols indicate
 general area of convection thought to initiate surge events in Stensrud et al. (1997).



722 Figure 2. Core NAM region with the model domain outlined (trapezoid). Also depicted are the
 724 three ISS sites (large circles): Puerto Penasco (PP), Bahía Kino (BK) and Los Mochis (LM).
 726 AG1, AG2, AC1, AC2, AC3, and AC4 denote the along-gulf and across-gulf cross-section
 locations respectively.

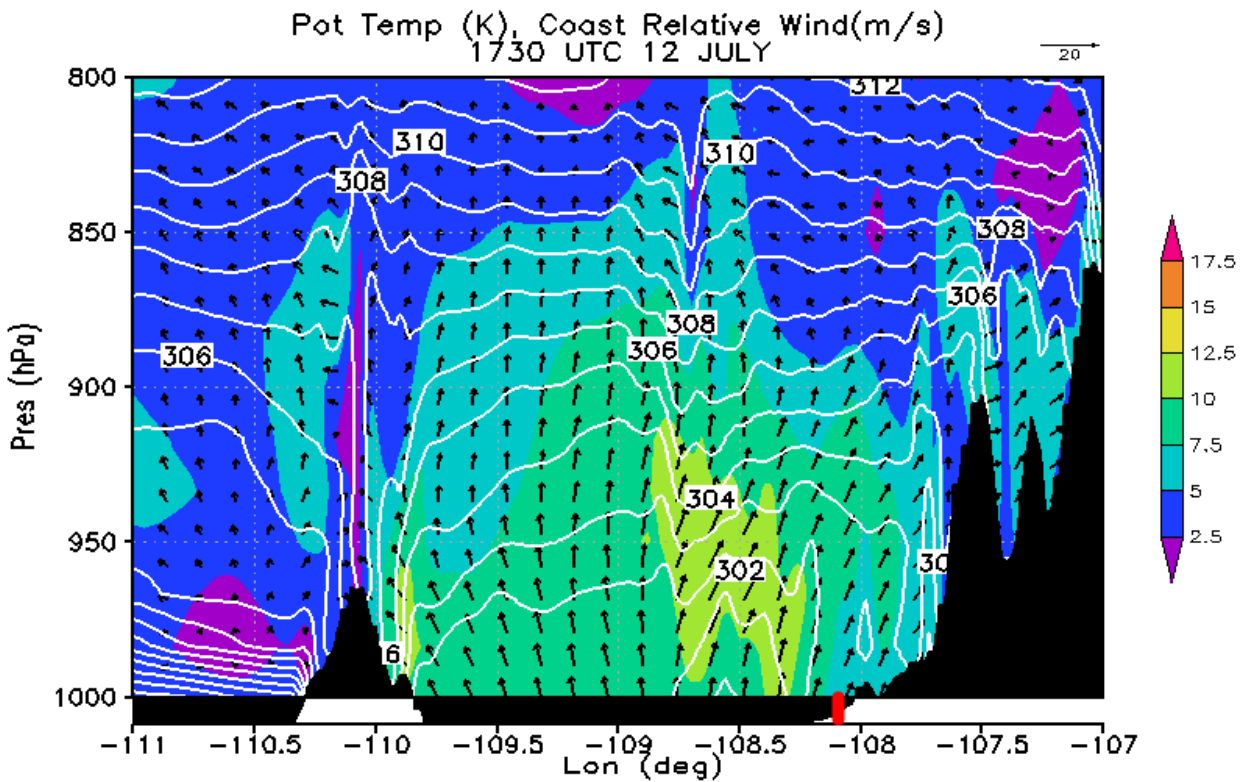


728 Figure 3. Progression of the leading edge of S2 and the gulf surge in the simulation. Times
 730 depicted are 1000, 1200, 1400, 1600, 1800, and 2000 UTC 12 July for S2 (dashed lines) and
 0300, 0500, 0700, 0900, 1100, and 1300 UTC 13 July for the gulf surge (solid lines). The lines
 progress from light to dark in chronological order.

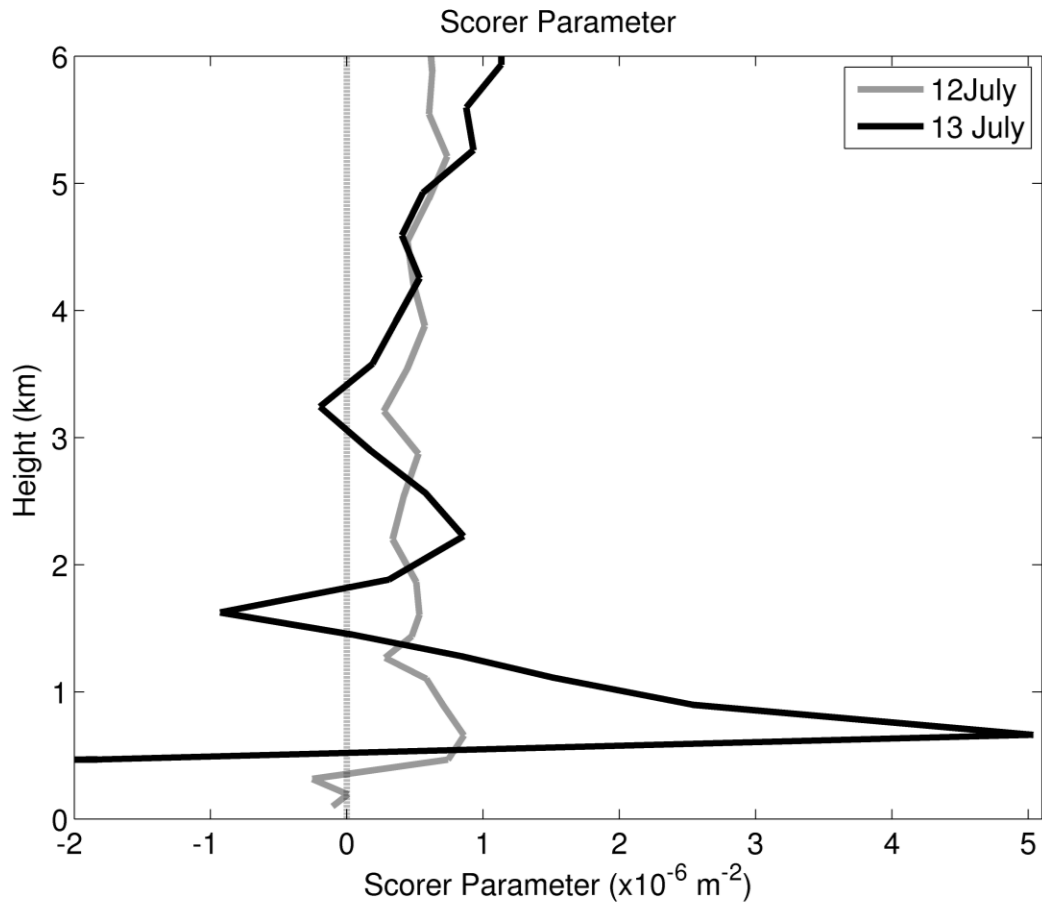


734

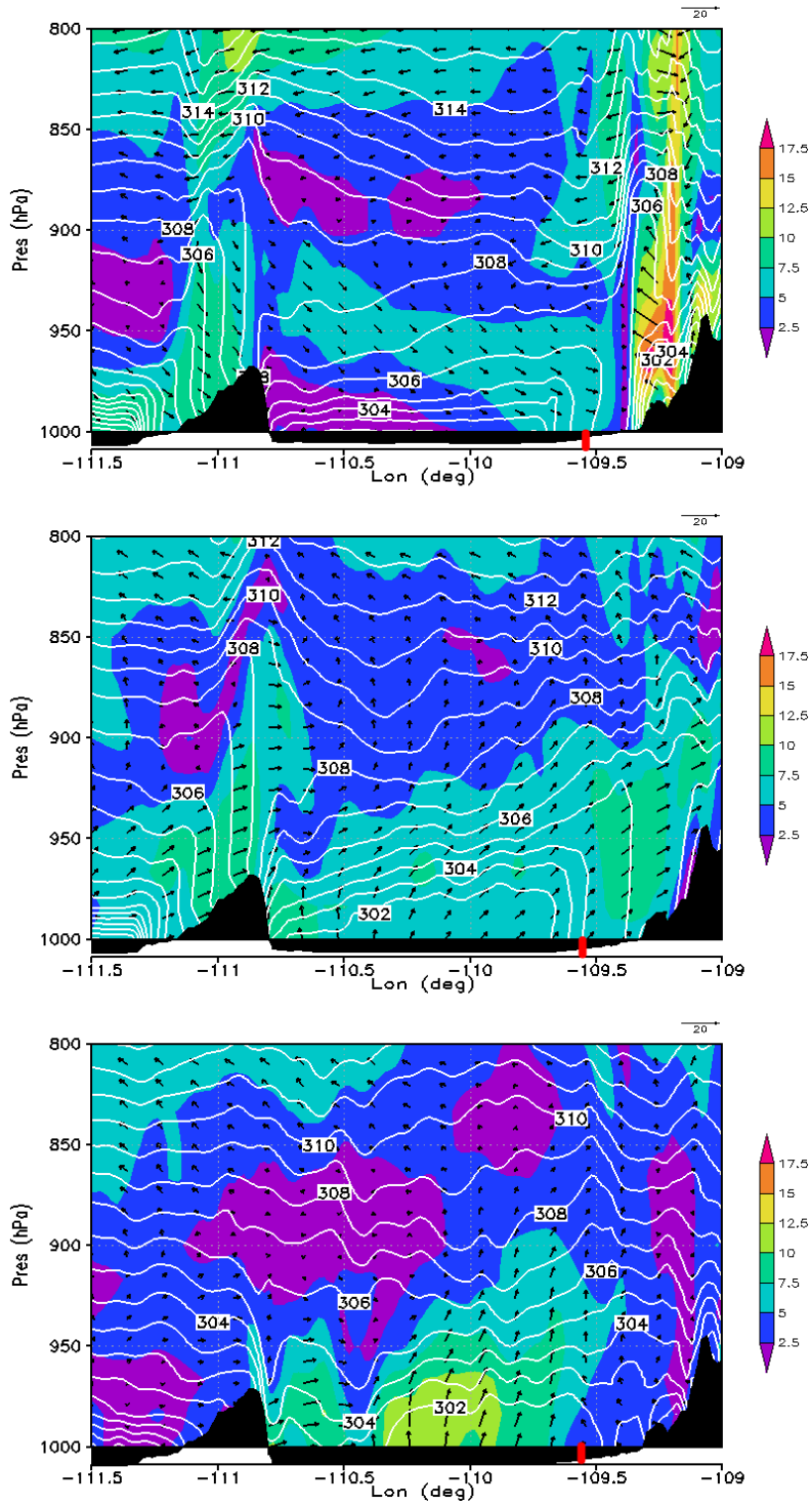
736 Figure 4. Potential temperature (K, black lines), moisture flux ($\text{g m kg}^{-1} \text{ s}^{-1}$, shading) and coast
 738 relative moisture flux vectors (arrows) at 1600 UTC (top) and 2000 UTC (bottom) 12 July 2004
 along AG1. S1 denotes cold pool associated with convection near GoC entrance, S2 denotes
 deeper disturbance discussed in Mejia et al. (2010). Red lines give general boundaries of S1 and
 S2.



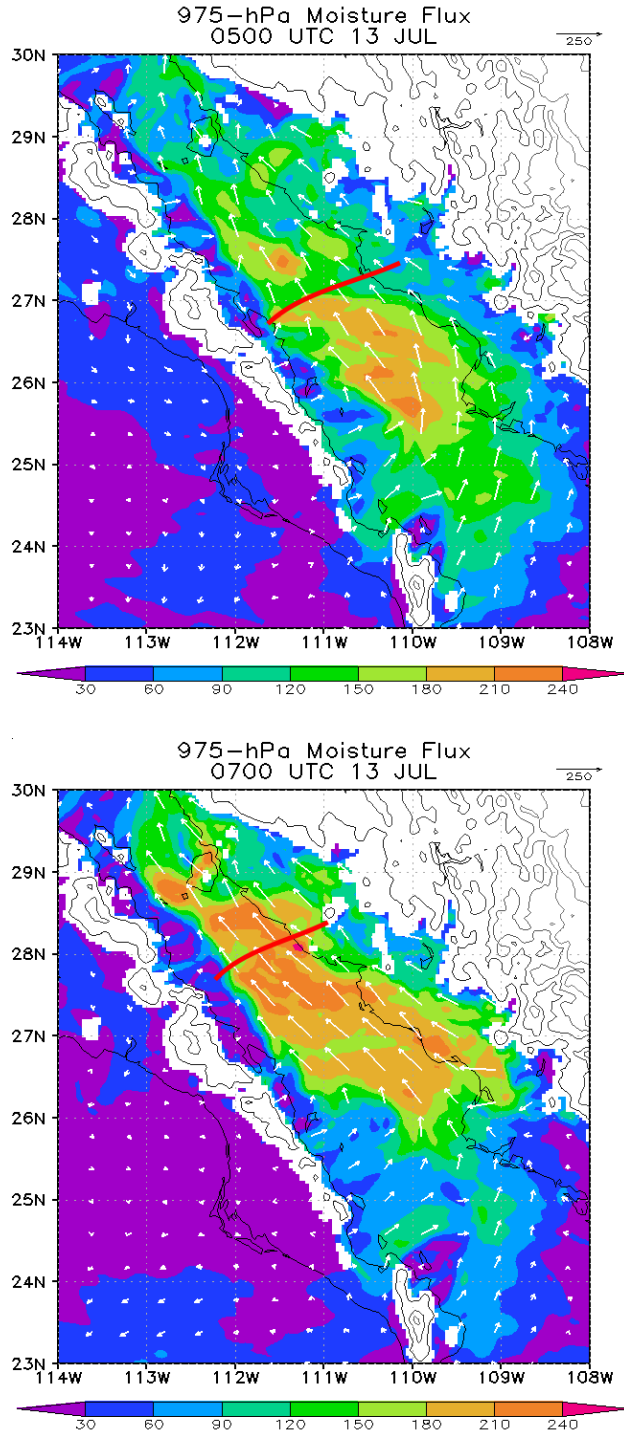
742 Figure 5. Simulated potential temperature (K, white contours), wind magnitude (m s^{-1} , shading)
 744 and coast relative wind vectors (arrows) along cross-gulf cross section AC1 at 1730 UTC 12
 July. Black shading indicates topography, while the red line indicates the coastline.



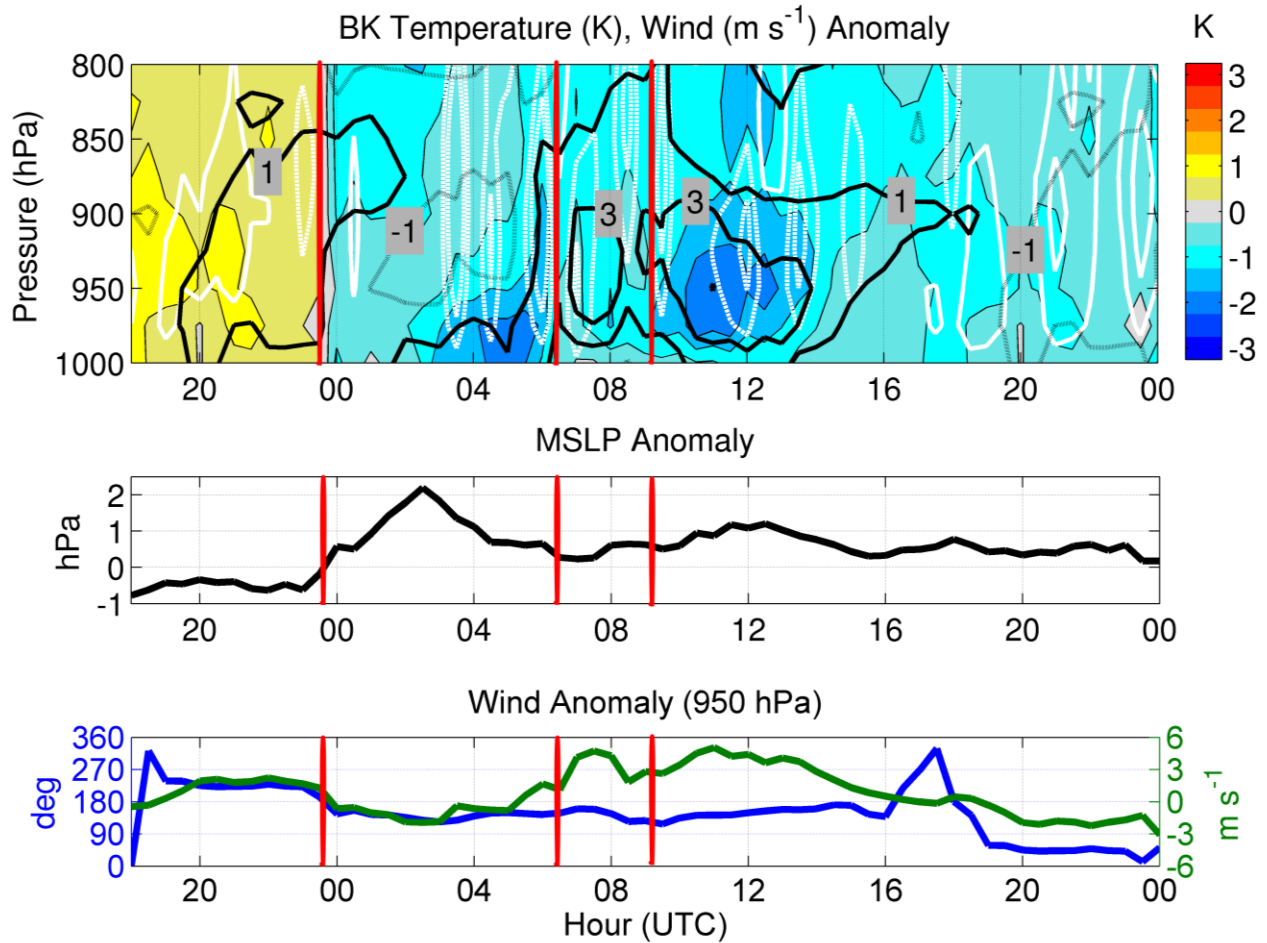
746 Figure 6. Vertical profile of the Scorer parameter at 1300 UTC 12 July ahead of S2 (solid gray
 748 line) and at 0600 UTC 13 July (black line) ahead of the surge.



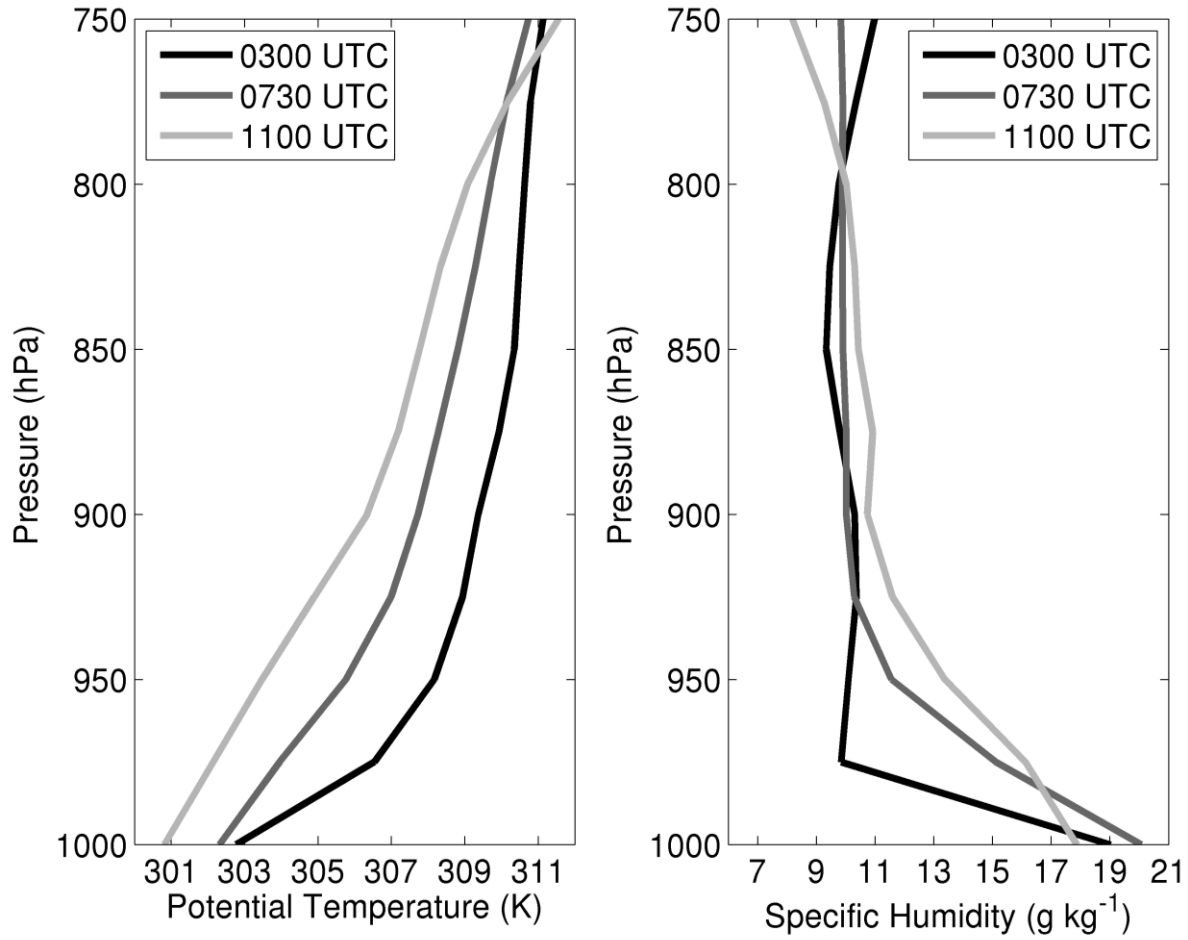
750 Figure 7. Simulated potential temperature (K, white contours), wind magnitude (m s^{-1} , shading)
 752 and coast relative wind vectors (arrows) taken along cross-gulf cross section AC2 at 0000 UTC
 754 12 July (top), 0000 UTC (middle), and 0500 UTC 13 July (bottom). Black shading indicates
 topography, while the red line indicates the coastline.



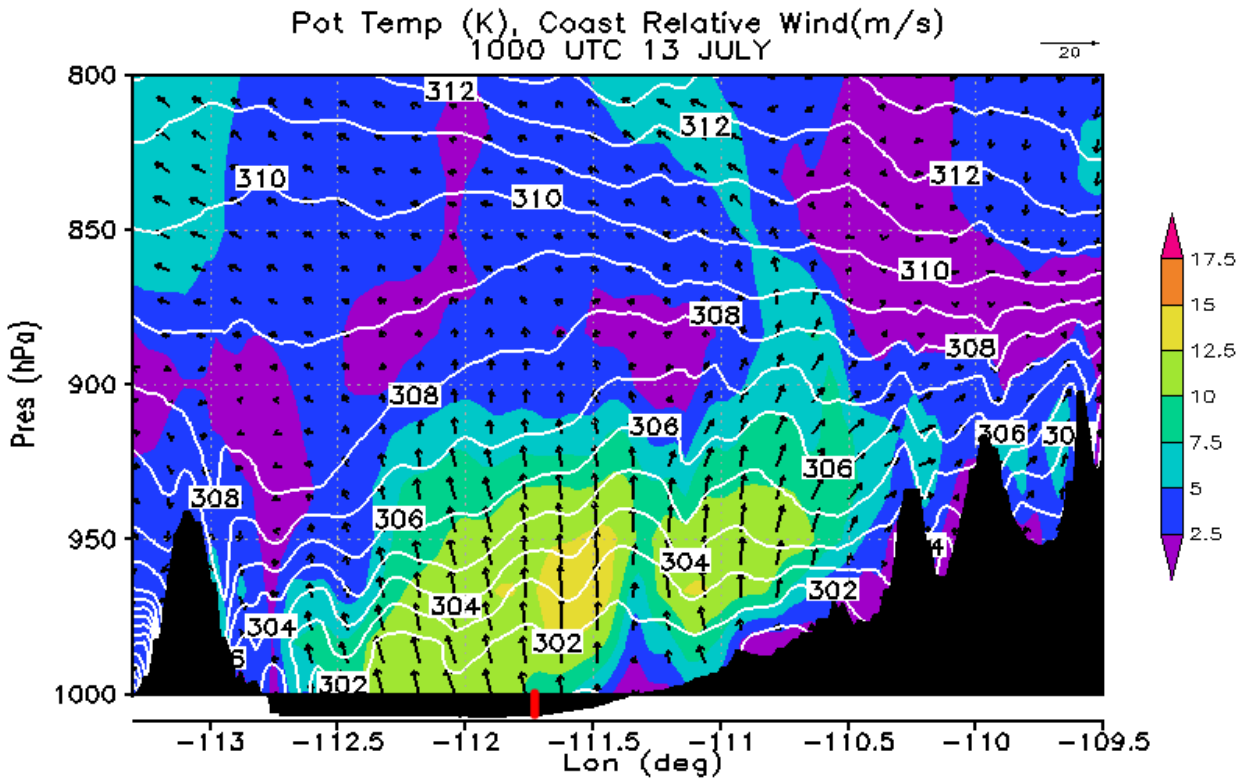
756 Figure 8. 975 hPa moisture flux ($\text{g m kg}^{-1} \text{s}^{-1}$) at 0500 (top) and 0700 (bottom) UTC 13 July.
 758 The red lines denote the approximate position of the surge leading edge.



760 Figure 9. Bahia Kino temperature anomalies (K, shading), wind anomalies (m s^{-1} , black
 762 contours), and vertical velocity (Pa s^{-1} , white contours: dashed upward, contour interval 0.5 Pa s^{-1})
 764 in the top panel. Mean Sea Level Pressure (MSLP) anomalies (hPa) in the middle panel. 950
 766 hPa wind speed (m s^{-1}) and direction anomalies (deg) in the bottom panel. All panels are
 anomalies compared to the diurnal mean for the WRF simulation period 0000 UTC 12 July to
 0000 UTC 14 July and display 18 UTC 12 July – 00 UTC 14 July. Red vertical lines denote
 passage of sea breeze, minor bore, and gulf surge event in chronological order.



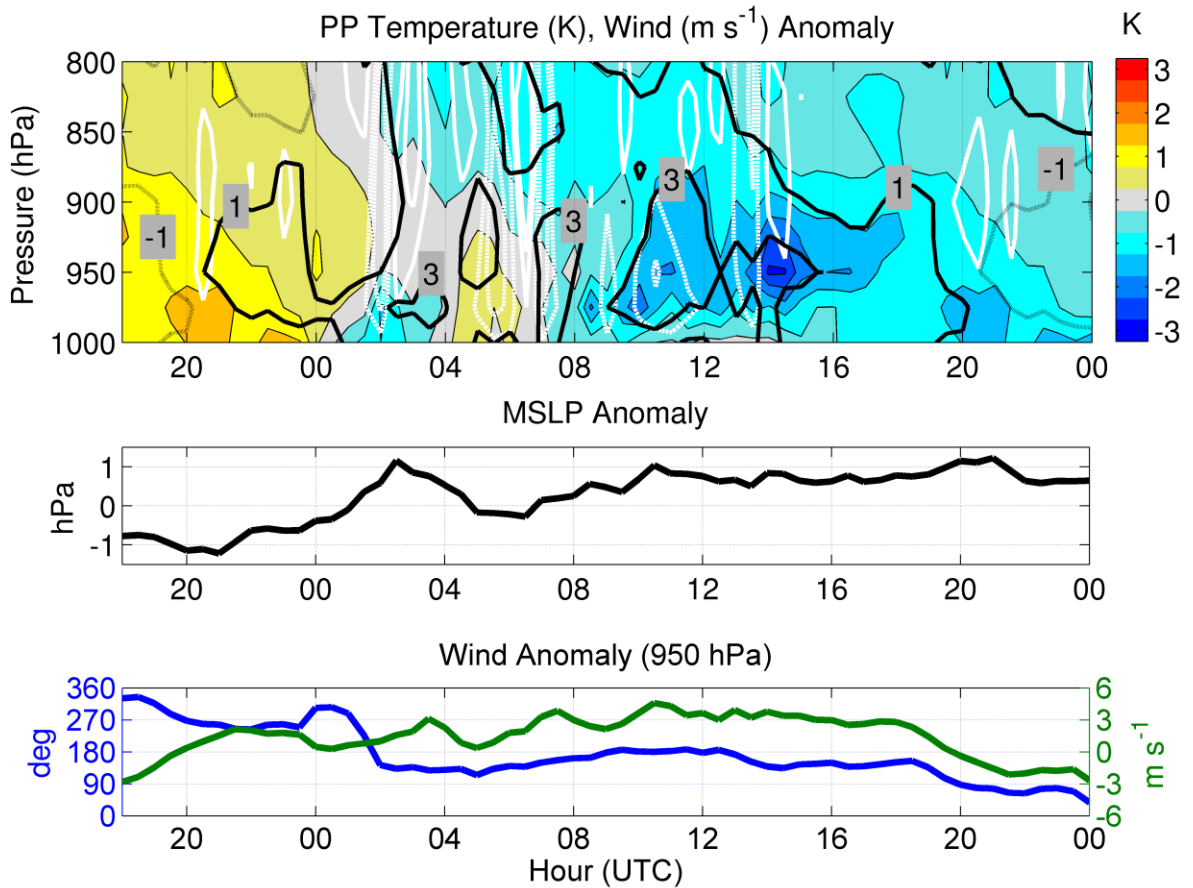
768 Figure 10. Potential temperature (K) (a) and mixing ratio (g kg^{-1}) (b) for the surge event at Bahia
 770 Kino at 0300 (black), 0730 (med. gray) and 1100 (light gray) UTC 13 July.



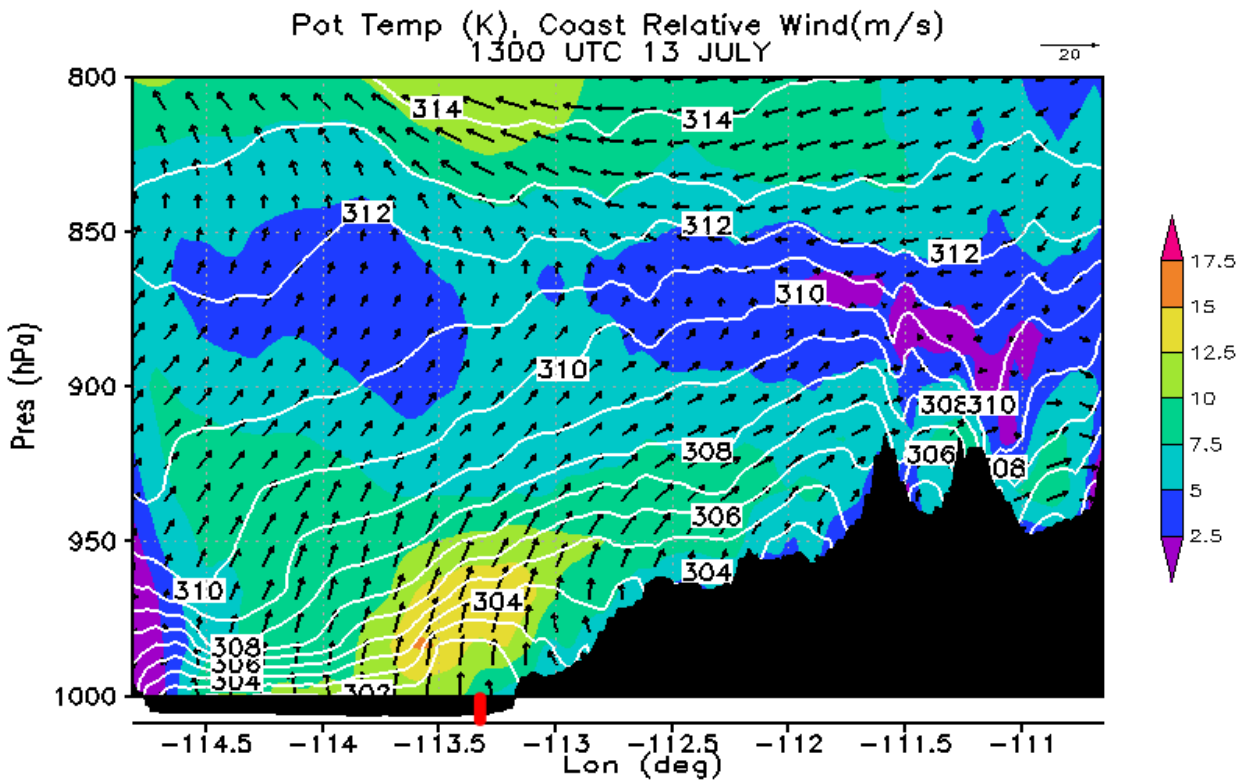
772 Figure 11. Simulated potential temperature (K, white contours), wind magnitude (m s^{-1} , shading)
 774 and coast relative wind vectors (arrows) taken along across-gulf cross section AC3 at 1000 UTC
 13 July (top). Black shading indicates topography, while the red line indicates the coastline.

776

778



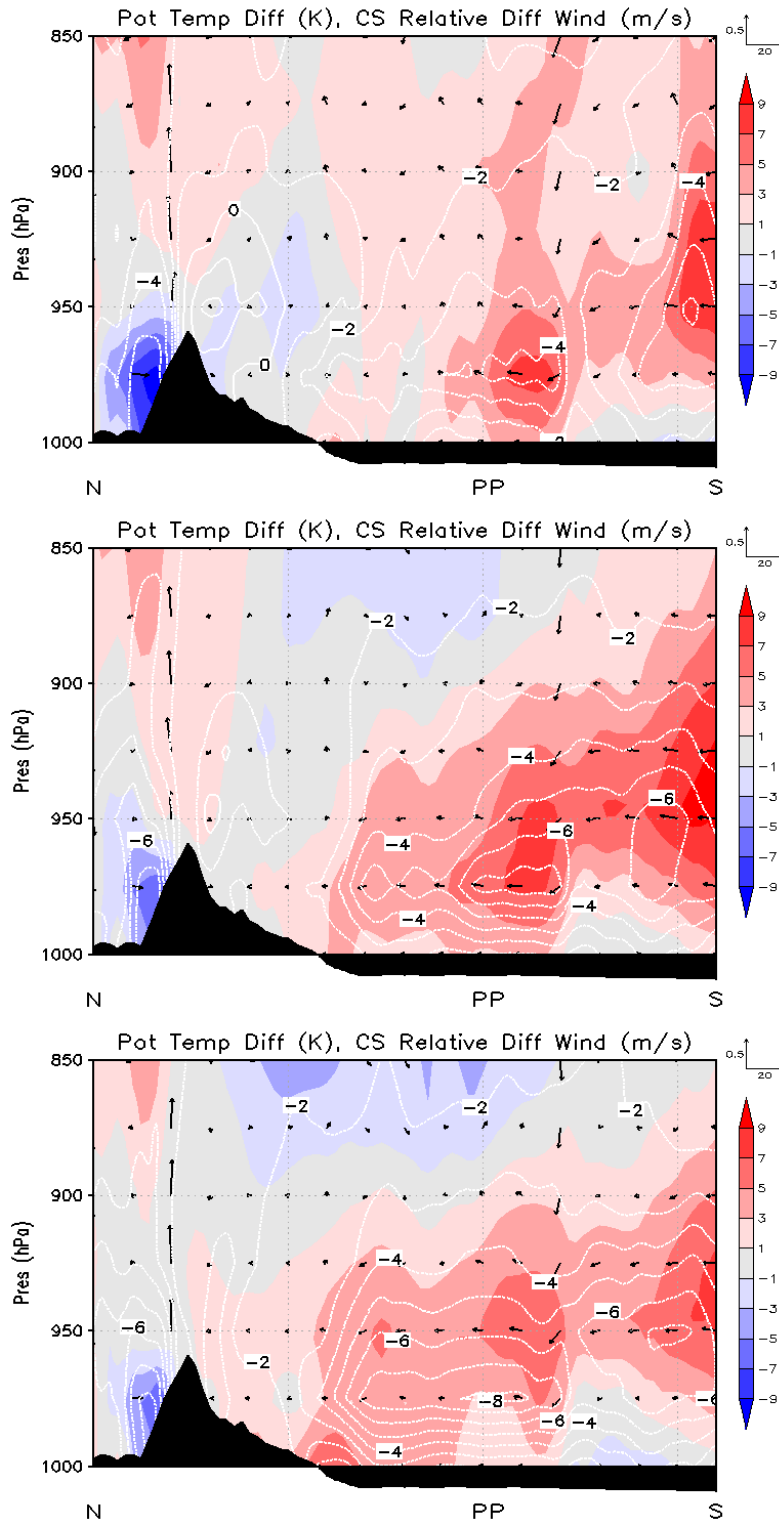
780 Figure 12. Puerto Penasco temperature anomalies (K, shading), wind anomalies (m s^{-1} , black
 782 contours), and vertical velocity (Pa s^{-1} , white contours: dashed upward, contour interval 0.5 Pa s^{-1}) in the top panel. Mean Sea Level Pressure (MSLP) anomalies (hPa) in the middle panel. 950
 784 hPa wind speed (m s^{-1}) and direction anomalies (deg) in the bottom panel. All panels are anomalies compared to the diurnal mean for the WRF simulation period 0000 UTC 12 July to 0000 UTC 14 July and display 18 UTC 12 July -00 UTC 14 July.



786

788

Figure 13. Simulated potential temperature (K, white contours), wind magnitude (m s^{-1} , shading) and coast relative wind vectors (arrows) taken along across-gulf cross section AC4 at 1300 UTC 13 July (top). Black shading indicates topography, while the red line indicates the coastline.



790

792

794

Figure 14. Potential temperature differences (white contours) and along cross section wind differences (arrows and shading) along AG2 on 13 July. Differences are taken as 1030 UTC – 0500 UTC (top panel), 1300 UTC – 0500 UTC (middle panel), 1430 – 0500 UTC (bottom panel).